American Mineralogist, Volume 85, pages xxx–xxx, 2000

Oxidation-reduction mechanism of iron in dioctahedral smectites: 1. Crystal chemistry of oxidized reference nontronites

A. MANCEAU,[1,*] B. LANSON,[1] V.A. DRITS[1,†] D. CHATEIGNER,[2] W.P. GATES,[3,‡,§] J. WU,[3] D. HUO,[3] AND J. W. STUCKI[3]

[1]Environmental Geochemistry Group, LGIT-IRIGM, University Joseph Fourier and CNRS, 38041 Grenoble Cedex 9, France
[2]LPEC, Université du Maine-Le Mans, av. Olivier Messiaen, BP535 72085 Le Mans cedex, France
[3]Department of Natural Resources and Environmental Sciences, University of Illinois, W-317 Turner Hall, 1102 South Goodwin Avenue, Urbana, Illinois 61801, U.S.A.

ABSTRACT

The crystal chemistry of Fe in four nontronites (Garfield, Panamint Valley, SWa-1, and NG-1) was investigated by chemical analysis, X-ray goniometry, X-ray absorption pre-edge spectroscopy, powder and polarized extended X-ray absorption fine structure (EXAFS, P-EXAFS) spectroscopy, and X-ray diffraction. The four reference nontronites have Fe/(Fe + Al + Mg) ratios ranging from 0.58 to 0.78, and are therefore representative of the different chemical compositions of dioctahedral ferruginous smectites. Pre-edge and powder EXAFS spectroscopy indicate that NG-1 contains 14 to 20% of tetrahedrally coordinated Fe^{3+}, whereas the other three samples have no detectable $^{IV}Fe^{3+}$. The partitioning of $^{VI}Fe^{3+}$ between cis (M2) and trans (M1) sites within the octahedral sheet was determined from the simulation of X-ray diffraction patterns for turbostratic nontronite crystallites by varying the site occupancy of Fe. Based on this analysis, the four nontronite samples are shown to be trans-vacant within the detection limit of 5% of total iron. The in-plane and out-of-plane local structure around Fe atoms was probed by angular P-EXAFS measurements performed on highly oriented, self-supporting films of each nontronite. The degree of parallel orientation of the clay layers in these films was determined by texture goniometry, in which the half width at half maximum of the deviation of the *c** axis of individual crystallites from the film plane normal, was found to be 9.9° for Garfield and 19° for SWa-1. These narrow distributions of orientation allowed us to treat the self-supporting films as single crystals during the quantitative analysis of polarized EXAFS spectra. The results from P-EXAFS, and from infrared spectroscopy (Madejova et al. 1994), were used to build a two-dimensional model for the distribution of Fe, and (Al,Mg) in sample SWa-l. In this nontronite, Fe, Al, and Mg atoms are statistically distributed within the octahedral sheet, but they exhibit some tendency toward local ordering. Fe-Fe and (Al, Mg)-(Al,Mg) pairs are preferentially aligned along the [010] direction and Fe-(Al,Mg) pairs along the [3$\bar{1}$0], and [$\bar{3}$10] directions. This distribution is compatible with the existence of small Fe domains separated by (Al,Mg), and empty octahedra, which segregation may account for the lack of magnetic ordering observed for this sample at low temperature (5 K) (Lear and Stucki 1990).

INTRODUCTION

Nontronite is a hydrous Fe^{3+}-bearing dioctahedral phyllosilicate that occurs widely in soils, weathering formations, and sediments. Its structure and chemical reactivity are reviewed by Güven (1991) and Stucki (1988). The general structural formula for nontronite is $(Si_{8-x-y}Al_xFe^{3+}_y)_{Tet}(Fe^{3+}_{4-z}Al_z)Oct\ Ex^{+}_{x+y}O_{20}(OH)_4 \cdot nH_2O$, where Tet, Oct, and Ex represent tetrahedral, octahedral, and interlayer cations. Nontronite is a 2:1 clay mineral, and thus contains two tetrahedral sheets per octahedral sheet (Fig. 1a). Tetrahedral sites are predominantly filled by Si ions but substitutions of Al, and occasionally of Fe^{3+}, can occur. Octahedral sites contain predominantly Fe^{3+}, with Al and a minor amount of Mg. The octahedral sheet has two different sites denoted M1 and M2. M1 is the trans octahedron with OH groups located at opposing corners whereas M2 is the cis octahedron with the two OH groups located on the same edge (Fig. 1a). Only two of the three octahedral positions per half unit cell (2 M2 + M1) are occupied, which can be either the two M2 sites (denoted herein as trans-vacant, tv), or the M1 and one of the two symmetrically independent M2 sites (denoted herein as cis-vacant, cv).

*E-mail: Alain.Manceau@obs.ujf-grenoble.fr
†And Geological Institute of the Russian Academy of Sciences, 7 Pyzhevsky Street, 109017 Moscow, Russia.
‡And Environmental Geochemistry Group, Grenoble.
§Present address: CSIRO Land and Water, Private Mail Bag No. 2, Glen Osmond, SA 5064, Australia

Structure determination of dioctahedral smectites are difficult because of the high density of physical defects (stacking faults, mixed-layering) and crystal chemical variability (isomorphous substitutions, site partitioning, different layer charges), requiring as many different methods as possible to reduce ambiguity. This study applies X-ray absorption pre-edge spectroscopy, X-ray diffraction, X-ray texture goniometry and polarized extended X-ray absorption fine structure (EXAFS) to four nontronites. The aim is to quantity the partitioning of Fe^{3+} among tetrahedral and octahedral sites, cis- and trans-octahedral sites, and the relative distribution of all octahedral cations (Fe^{3+}, Mg, Al) among octahedral sites.

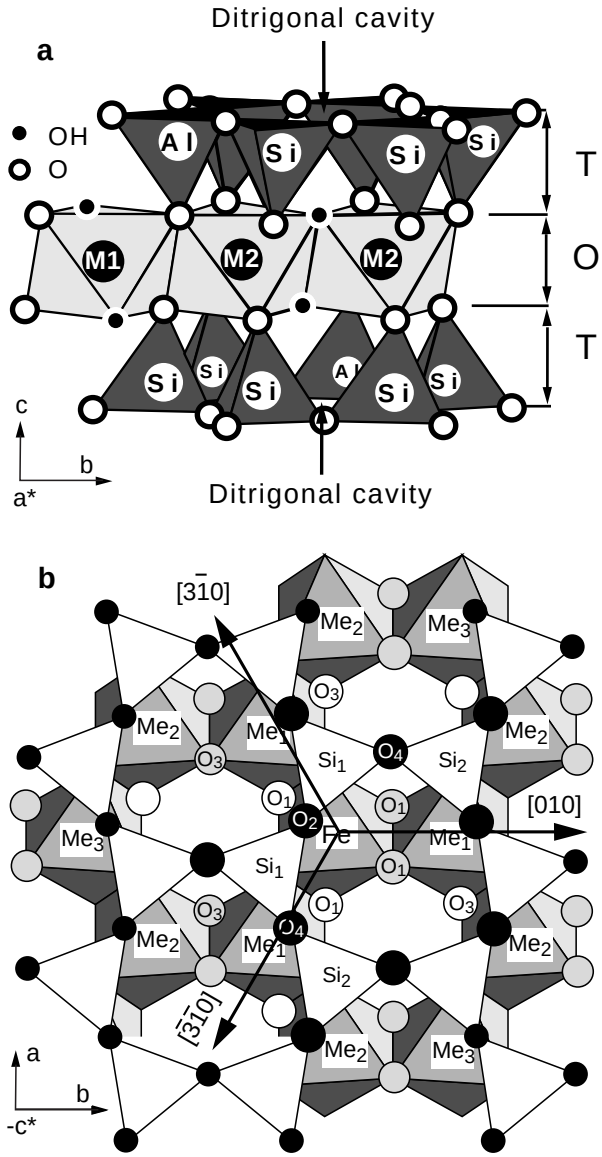

FIGURE 1. (**a**) Idealized structure of nontronite. T: tetrahedral sheet, O: octahedral sheet. M1 denotes trans sites, M2, cis sites. One of the three octahedral sites are unoccupied. (**b**) Projection down *c** of a dioctahedral layer silicate (one tetrahedral sheet is not shown), and representation of the successive atomic shells around a central Fe atom. Blank triangles are (Si,Al)O4 tetrahedra, black atoms are basal O atoms, blank atoms are O atoms from the octahedral sheet, and greyed atoms are OH groups. Si labels stand indifferently for Si and Al atoms, Me is an octahedral cation (Fe, Al, or Mg).

PREVIOUS WORK

Ferric iron is the dominant cation in the octahedral sheet of nontronite, but the substitution of $^{IV}Fe^{3+}$ for ^{IV}Si or ^{IV}Al is possible, and is often arbitrarily assumed to balance structural formulae when the chemical analysis reveals an excess of Fe and a concomitant deficit of Al. This assumption is likely invalid in many natural samples unless great care is taken to remove Fe oxide impurities that are generally intimately associated as surface coatings or separate grains (Güven 1991; Murad 1987). Mössbauer spectroscopy has been used to help identify tetrahedral Fe, with amounts of $^{IV}Fe^{3+}$ as great as 12–32% of total Fe being reported for some nontronite samples (Goodman et al. 1976). The results are equivocal because Mössbauer doublets are often poorly resolved. For instance, Besson et al. (1983) and Murad et al. (1990) reported 6 to 9% of $^{IV}Fe^{3+}$ in Garfield nontronite, whereas Bonnin et al. (1985) concluded that $^{IV}Fe^{3+}$ amounts to less than 1% of total Fe.

Oblique texture electron diffraction and X-ray diffraction showed that in Fe^{3+}-rich dioctahedral smectites Fe fills cis sites (Tsipursky et al. 1978, 1985; Besson et al. 1983; Tsipursky and Drits 1984; Sakharov et al. 1990). The octahedral site occupancy of Fe^{3+} in nontronites has been indirectly inferred from magnetism measurements, from which up to 13% of $^{VI}Fe^{3+}$ were allowed in trans sites (Lear and Stucki 1990). This interpretation is reasonably compatible with the crystallographic observations by Besson et al. (1983) and Tsipursky and Drits (1984) because the accuracy in the determination of the Fe site occupancy by electron and X-ray diffraction was about 10% of total octahedral Fe^{3+}. However, the presence of trans Fe^{3+}, in addition to cis Fe^{3+}, is generally unfavorable from a crystal chemical point of view as it violates the principe of local charge balance. Indirect evidence for the absence of coexisting cis- and trans-occupied sites *within the same octahedral sheet* is found in recent results on the distribution of octahedral cations in illites and illite-smectites (McCarthy and Reynolds 1995; Drits and McCarty 1996; Drits et al. 1996), where exclusively cis and trans sites belong to different layers.

The order-disorder of isomorphous octahedral cations in dioctahedral smectites has also been investigated by a number of methods. Whereas X-ray diffraction is sensitive to average site occupancies, spectroscopic methods reveal information regarding the local distribution of cations. The nature and number of cationic pairs bonded to OH groups have been determined in dioctahedral phyllosilicates and smectites by infrared (IR) spectroscopy (Besson and Drits 1997a, 1997b; Besson et al. 1987; Madejova et al. 1994; Slonimskaya et al. 1986). These studies showed that the distribution of Al, Fe^{2+}, Fe^{3+}, and Mg is not completely disordered, and that, in general, Fe^{3+}-Al pairs have a lower probability of occurrence than predicted by statistical distribution. By combining XRD, EXAFS, IR, Mössbauer, and computer simulations, Drits et al. (1997) found that in celadonites, glauconites, and Fe-illites octahedral cations are distributed in domains of variable size, chemical composition, and cation or-

dering. Muller et al. (1997) showed from XRD, EXAFS, and IR that Fe and Mg are segregated in small clusters in the aluminous octahedral sheet of the Camp-Bertaux montmorillonite.

THEORETICAL BACKGROUND

Polarized EXAFS (P-EXAFS) is a new technique (Manceau et al. 1998, 1999), and its principles and application to clay mineral structures is described briefly. The angular dependence of the EXAFS contribution for a given atomic pair (*ij*), and at the K-edge of the X-ray absorber *i*, is written in the plane wave approximation:

$$\chi_{ij}(k,\theta) = 3 \langle\cos^2\theta_{ij}\rangle \chi_{ij}^{iso}(k) = \sum_{j=1}^{N_{cryst}} (3\cos^2\theta_{ij})\ \chi_{ij}^{iso}(k) \qquad (1)$$

where θ_{ij} is the angle between the electric field vector ε and the vector $\boldsymbol{R}_{ij}$ that connects the absorbing *i* atom to the backscattering *j* atom, and χ_{ij}^{iso} is the isotropic contribution of the *j* shell. The summation is made over all the N_{cryst} atoms of the *j* shell because, for some orientations of ε, atoms may not have the same spatial position, and thus θ angle. For a true powder (i.e., perfectly random crystallites), there is no angular variation, and $3 \langle\cos^2\theta_{ij}\rangle = 1$.

From Equation 1, neighboring *j* atoms located along the polarization direction ($\theta = 0°$) are preferentially probed, whereas atoms located in a plane perpendicular to ε ($\theta = 90°$) are not observed. Thus P-EXAFS measurements provide orientational information, and can be used to probe the local structure of layer silicates between two different directional limits, parallel and perpendicular to the (001) plane, by varying the angle between ε and the layer plane of a single crystal or the surface of a self-supporting clay film. For a film, individual clay platelets have their *a* and *b* axes randomly distributed around the normal to the film plane and, consequently, θ_{ij} varies from one crystallite to another. Thus, this formula must be transformed through the introduction of angles that are independent of the orientation of layers in the film plane. Utilizing the axisymmetrical symmetry of self-supporting clay films, and assuming that individual platelets have their (001) basal surface perfectly aligned parallel to the film plane, one can write (Manceau et al. 1998):

$$\langle\cos^2\theta\rangle = \cos^2\beta \sin^2\alpha + (\sin^2\beta \cos^2\alpha)/2 \qquad (2)$$

where α is the angle between ε and the film plane (i.e., the experimental angle), and β is the angle between $\boldsymbol{R}_{ij}$ and the film normal. This polarization term is independent of the relative position of crystallites in the film plane, and of the variation of θ_{ij} from one atom to another in the *j* shell. The amplitude of $\chi_{ij}^{iso}(k)$ is obviously proportional to N_{cryst}, and in a polarized experiment one detects an apparent number of neighbors, which is the effective number (N_{eff}) of atoms really seen at the α angle. Then:

$$\chi_{ij}(k,\alpha) = \frac{N_{eff}}{N_{cryst}} \chi_{ij}^{iso}(k) \qquad (3)$$

with

$$N_{eff} = 3\, N_{cryst} [\ \cos^2\beta \sin^2\alpha + (\sin^2\beta \cos^2\alpha)/2\ ] \qquad (4)$$

For normal ($\alpha = 90°$) and parallel ($\alpha = 0°$) orientations, (4) reduces to:

$$N_{eff}^{\parallel} = \frac{3}{2} N_{cryst} \sin^2\beta \qquad (5)$$

$$N_{eff}^{\perp} = 3 N_{cryst} \cos^2\beta \qquad (6)$$

From knowledge of the crystallographic β angle of a *j* shell, calculation of the effective number of neighbors seen in a P-EXAFS experiment for the two independent orientations is possible. Conversely, β in an unknown structure can be deduced from N_{eff} determined from the simulation of P-EXAFS spectra. For the magic angle of $\beta = 54.7°$, $N_{eff}^{\perp} = N_{eff}^{\parallel} = N_{cryst}$, the atomic pair has no polarization dependence in the X-ray beam, and the absorption amplitude is constant and equal to that of powders [$\chi_{ij}(k,\alpha) = \chi_{ij}^{iso}(k)$]. For $\beta < 54.7°$, $\chi_{ij}(k,\alpha)$ increases with α, whereas for $\beta > 54.7°$, $\chi_{ij}(k,\alpha)$ decreases with increasing α.

Equations 2 to 6 presume that individual platelets have their (001) basal surface perfectly aligned parallel to the film plane; otherwise, if dispersion from this orientation occurs, *N* determined from experimental EXAFS spectra (N_{exafs}) would be intermediate between N_{eff} and N_{cryst}. With smectitic clays, self-supporting films can be prepared in which the crystallite dispersion has a half width at half maximum (HWHM) of ~10° (Manceau et al. 1998). In this case, dispersion of the *c** axis around the film normal can be neglected and $N_{exafs} \approx N_{eff}$ (Manceau et al. 1999).

We now apply these theoretical considerations to nontronite. Interatomic distances (*R*), β angles, N_{cryst}, $N_{eff}^{\parallel}$, and $N_{eff}^{\perp}$ for the successive atomic shells located at increasing distance from Fe atoms in Garfield nontronite (Fig. 1b) are listed in Table 1. In phyllosilicates, the nearest octahedral (Oct1) and tetrahedral (Tet1) cationic shells are located about the same distance from Fe atoms (~3.04–3.10 Å vs. ~3.25–3.30 Å), and their EXAFS contributions strongly overlap, which reduces the precision of the quantitative analysis of EXAFS spectra (Manceau 1990). Inspection of Figure 1b and Table 1 reveals that using P-EXAFS in the context of phyllosilicates has the advantage of canceling Fe-Oct1 pairs [$N_{eff}^{\perp}$[Fe-(Fe,Al,Mg)$_1$] = 0) and selecting Fe-Tet1 pairs [($N_{eff}^{\perp}$(Fe-(Si,Al)] = 8.6) in the normal orientation. Conversely, when the polarization vector is in the film plane, the Fe-Oct1 contribution is reinforced ($N_{eff}^{\parallel} = 4.5$), and the Fe-Tet1 is small ($N_{eff}^{\parallel} = 1.7$). Thus, the residual Fe-Tet1 contribution at $\alpha = 0°$ equals 1.7/8.6 = 20% of its amplitude at $\alpha = 90°$ and, therefore, the Fe-Oct1 contribution can be singled out from the in-plane EXAFS spectrum by subtracting the residual Fe-Tet1 component. The filtering of the Fe-Oct1 and Fe-Tet1 contributions in P-EXAFS experiments enhances the precision on N_{Oct1} (Oct = Fe, Al, Mg…) by supressing the three adjustable struc-

TABLE 1. Angular dependence of atomic shell contributions for Garfield nontronite in polarized EXAFS

Atom	Label	*R* (Å)	<β>	N_{cyst}	$N_{eff}^{\parallel}$	$N_{eff}^{\perp}$
O1		1.97-2.04	57°	6	6.3	5.3
Fe1	Oct1	3.05	90°	3	4.5	0
$(Si,Al)_1$	Tet1	3.26	32°	4	1.7	8.6
O2		3.45	11°	2	0.1	5.8
O3		3.74	73°	6	8.2	1.5
O4		4.03-4.21	37°	4	2.2	7.6
$(Si,Al)_2$	Tet2	4.49	52°	4	3.7	4.5
Fe2	Oct2	5.28	90°	6	9	0
Fe3	Oct3	6.10	90°	3	4.5	0

tural parameters of the tetrahedral contribution in the spectral fit (N_{Tet1}, R_{Tet1}, and the Debye-Waller factor σ_{Tet1}). Also, in parallel orientation the total wave amplitude of $\chi_{Fe\text{-}Oct1}(k)$ is enhanced by 50% as compared to $\chi^{iso}_{Fe\text{-}Oct1}$ because $N_{eff} = 1.5\ N_{cryst}$ (Eq. 5). This magnification of the electronic wave amplitude, and the filtering of the Fe-Tet1 pair contribution, greatly contributes to increasing the sensitivity of EXAFS for studying the distribution of Fe-Fe and Fe-(Al,Mg) pairs in the octahedral sheet of layer silicates.

EXPERIMENTAL METHODS

Materials

Nontronite samples used in this study were from Garfield, Washington (Rachel Glaeser); Panamint Valley, California (PV, J.L. Post); Grant County, Washington (SWa-l, Source Clays Repository of The Clay Minerals Society, Columbia, Missouri); and Höhen Hagen, Germany (NG-1, Source Clays Repository of The Clay Minerals Society, Columbia, Missouri). Impurities were removed by performing successive sedimentations on the Na-saturated form in deionized water. NG-1 was also subjected to magnetic fractionation to remove finely divided maghemite and associated Fe-poor smectites (Lear et al. 1988). Chemical analyses were performed on all samples: (1) for Fe^{2+} and Fe^{3+} using the quantitative 1,10-phenanthroline method of Komadel and Stucki (1988); (2) for total Si using NaOH fusion, followed by silicomolybdous blue spectrometry at 820 nm (Hallmark et al. 1982); (3) for Al by the Aluminon (ammonium salt of aurinitricarboxylic acid) spectrophotometric method at 530 nm, after H_2SO_4+HF digestion (Barnhisel and Bertsch 1982); and (4) for total K, Na, Ca, and Mg by atomic absorption spectrophotometry using the same diluted digestate solutions prepared for Fe analysis. Structural formulae calculated on a $O_{20}(OH)_4$ basis are reported in Table 2. Highly oriented self-supporting films of uniform thickness were prepared by vacuum filtration and sedimentation (Manceau et al. 1998a).

Powder X-ray diffraction

Powder X-ray diffraction (XRD) patterns of nontronite samples were obtained using Cu*K*α radiation with a Siemens D5000 powder diffractometer equipped with a Kevex Si(Li) solid-state detector. Intensities were measured at an interval of 2θ 0.04° and 40–50 s counting times per step. The absolute precision of Bragg angles was better than 2θ 0.01° over the whole angular range. XRD patterns were recorded on air dried Na-saturated samples and dehydrated in a vacuum chamber ($P = 10^{-5}$ to 10^{-6} atm). The 02-11 and 20-13 two-dimensional diffraction bands of XRD patterns for dehydrated samples were simulated using the mathematical formalism described by Plançon (1981), Sakharov et al. (1982a, 1982b), and Drits and Tchoubar (1990). Random stacking in individual crystallites was assumed to be 100%, as in pure turbostratic layer compounds (Brindley and Brown 1980). Coherent scattering domains (CSDs) in the layer plane are disk shaped, with a mean radius determined for each sample by fitting the profile of the 02-11 band. For each sample, the fraction of the different octahedral species (Fe, Al, Mg) was taken from the chemical composition (Table 2). Values of $d(001)$, $b = 6d(060)$, and $a = b/\sqrt{3}$ were determined from experimental XRD patterns.

TABLE 2. Unit-cell formulae for nontronites calculated from chemical analysis

Sample	Cation composition per $O_{20}(OH)_4$	Tet net charge	Oct net charge
Garfield	$Na_{0.81}(Si_{7.22}Al_{0.78})(Fe^{3+}_{3.64}Fe^{2+}_{0.01}Al_{0.32}Mg_{0.04})$	–0.78	–0.02
PV	$Na_{0.89}(Si_{7.57}Al_{0.43})(Fe^{3+}_{2.87}Fe^{2+}_{0.01}Al_{0.65}Mg_{0.47})$	–0.43	–0.48
SWa-1	$Na_{0.87}(Si_{7.38}Al_{0.62})(Fe^{3+}_{2.67}Fe^{2+}_{0.01}Al_{1.08}Mg_{0.23})$	–0.62	–0.27
NG-1*	$Na_{0.70}(Si_{7.29}Fe^{3+}_{0.63}Al_{0.08})(Fe^{3+}_{3.08}Fe^{2+}_{0.01}Al_{0.88}Mg_{0.06})$	–0.71	+0.02

* Contains 17% of $^{IV}Fe^{3+}$ in agreement with EXAFS.

Texture goniometry

The quantitative determination of texture is based on the concept of orientation distribution (Bunge 1981), and represents the distribution of all possible orientations of all crystals (crystallites) constituting a polycrystalline aggregate (Matthies et al. 1987). Garfield measurements were reported in Manceau et al. (1998). The (004) pole figures for the three other nontronites were obtained by using a high resolution Seifert (PTS) four circle texture goniometer mounted on a Rigaku rotating anode, and with Cu*K*α monochromatized radiation. A 1 × 1 mm beam was collimated on the sample, and a 1 mm horizontal aperture was used for detection, giving no defocusing up to ρ = 50°. Possible sample inhomogeneity effects were reduced by continuously rotating the sample around its normal during the measurements. The (004) pole figures were measured using angle increments in tilt (ρ) and azimuth (φ) of 5° and for angular ranges of $0 \le \rho \le 85°$ and $0 \le \varphi \le 360°$. The full θ_{hkl}-$2\theta_{hkl}$ pattern was measured in the $1 \le \theta_{hkl} \le 35°$ interval. The scattering background under the diffracted 004 reflection was estimated by a 2nd order polynomial interpolation from an interval of 1° in 2θ on the right and left sides of the peak, and was subsequently subtracted from the experimental pattern to obtain the net diffracted intensity. This intensity was corrected for defocusing in the $50 \le \rho \le 75°$ range since $I = 0$ for $\rho > 75°$. The distribution of densities, $P(\rho)$, was then obtained by normalizing the previous intensities, $I(\rho)$, according to:

$$P(\rho) = \frac{I(\rho)}{N_{hkl}} \tag{7}$$

where N_{hkl} is the normalization factor calculated over all experimental points by

$$N_{hkl} = \sum_{\rho=0°}^{90°} I(\rho)\sin\rho \Big/ \sum_{\rho=0°}^{90°} \sin\rho \tag{8}$$

The sinρ factor takes into account the variations of the volume of the measured cells with the inclination of the sample (ρ).

Pre-edge

Fe K-edge measurements were performed on the D42 spectrometer at LURE (Orsay, France) in transmission mode with gas ionization chambers filled with an air/helium mixture dosed to attenuate the beam intensity by ~20% before and ~50% after sample entry. The DCI electron storage ring is a first generation synchrotron source, and the divergence of the incident beam is as high as 10^{-4} radians. The spectral resolution was improved by using a high *hkl* reflection [Si(331)] as the mono-

chromator. With this reflection the energy resolution was 1.5 eV, which is comparable to the Fe core level width of 1.1 to 1.2 eV (Muller et al. 1982). Pre-edge spectra were recorded at the magic angle to eliminate texture effects (Manceau et al. 1990), then normalized to the main absorption jump according to the procedure described by Manceau et al. (1997).

P-EXAFS

Data acquisition. Measurements on self-supporting films produce high quality EXAFS spectra (Manceau et al. 1998, 1999). This is due mainly to the small size of clay particles (<2 μm), which is smaller than one absorption length at the Fe *K*-edge (<40 μm), and to the homogenous and relative thinness ($\Delta\mu \approx 0.8$ at $\alpha = 60°$ for all samples) of clay films that ensured a precise measurement of the absorption coefficient (Lu and Stern 1983; Manceau and Gates 1997; Stern and Kim 1981). Angular measurements were performed by rotating the film layers around an axis normal to both the beam direction and ε at α angles equal to 0°, 20°, 35°, 50° and 60°. The out-of-plane $\chi(k,\alpha = 90°)$ function was calculated for each *k* value via linear regression as a function of $\cos^2\alpha$ and extrapolation to 90° (Manceau et al. 1988, 1999). P-EXAFS spectra were recorded over the 6900–7950 eV energy (*E*) range, which corresponds to $k_{max} = 14.5$ Å^{-1} and a Bragg angle variation from 46° to 38.5° with the Si(331) reflection. Over this angular range more than 99.9% of the synchrotron radiation is linearly polarized, being precisely 100% at the monochromator Bragg angle of 45° (Hazemann et al. 1992). Powder EXAFS spectra [$\chi(\alpha = 35°)$, Manceau et al. 1990] for Garfield, SWa-1, and NG-1 were recorded up to 8200 eV ($k_{max} = 16.5$ Å^{-1}) to increase the distance resolution limit of the method, and with a counting time of 20 s.

Data reduction. EXAFS spectra were analyzed according to standard procedures (Lengeler and Eisenberger 1980). A Kaiser function window (Manceau and Combes 1988) was used in the Fourier transform to minimize the intensity of side lobes (i.e., harmonic peaks) resulting from truncation effects (Teo 1986). With this function, secondary peak intensities are on the order of 5% of the intensity of main structural peaks (Manceau 1995). The resulting low intensity increases the sensitivity to less pronounced structural features in the radial structure function (RSF), and provides strong evidence that peak intensities above this value should be interpreted as being of structural origin. Fourier transforms were performed on *k*- or k^3-weighted EXAFS spectra to emphasize contributions from the lower or higher *k* region, respectively. The combination of these two *k*-space weighting treatments was particularly helpful in the analysis of contributions from overlapping atomic shells. The arguments presented in the results section are rather technical in some places, so for the sake of clarity, how these two *k*-space weightings preferentially modify the relative contributions of the various atomic shells in RSFs is explained below.

The EXAFS contribution of an *ij* atomic pair is written in the reciprocal *k* space by the wave function (Teo 1986):

$$\chi_{ij}(k,\theta) = \sum_{j=1}^{N_{cryst}} (3\cos^2\theta_{ij})(S_0^2 N_{cryst}/R_{ij}^2) F_j(k) \exp(-2\sigma_{ij}^2 k^2) \exp[-2R_{ij}/\lambda(k)] \sin[2kR_{ij} + \phi_{ij}(k)] \quad (9)$$

where S_0^2 is a many body term ($S_0^2 \sim 1$), F_j is the scattering amplitude function of the backscattering *j* atom, σ_{ij} is the Debye-Waller term, λ is the electron mean-free path, and ϕ_{ij} is the phase shift function for the *ij* pair. The contribution of this pair in real (*R*) space (i.e., in the RSF) is obtained by integrating $k\chi_{ij}$ (*k*-weighting) or $k^3\chi_{ij}$ (k^3-weighting) over *k* during the Fourier transform (FT).

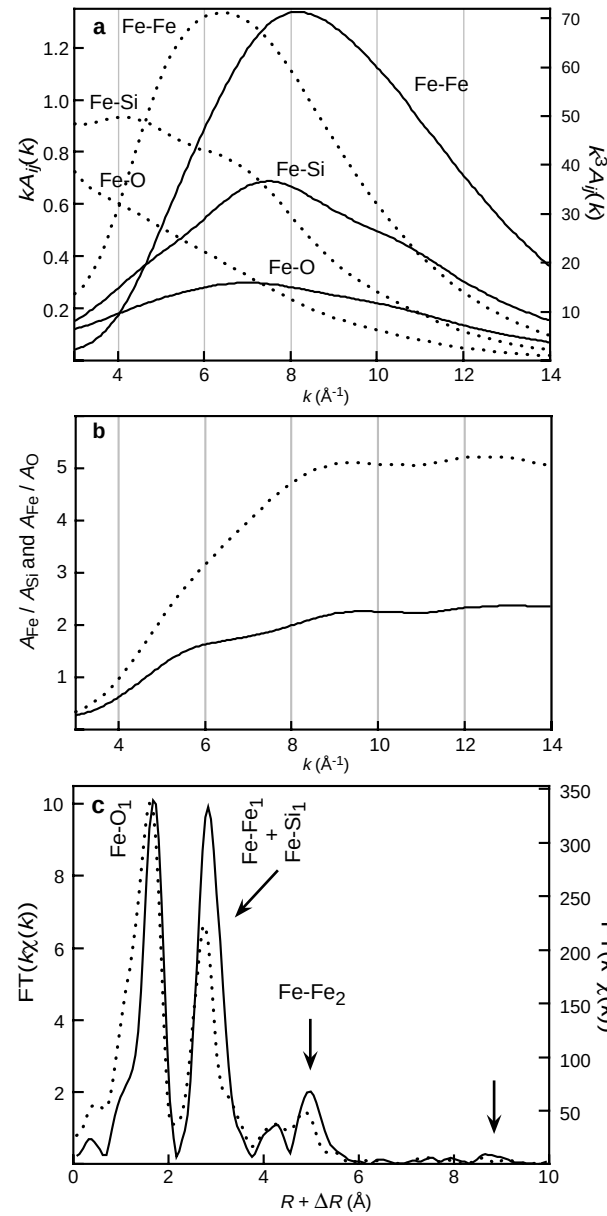

FIGURE 2. (**a**) *k*- and k^3-weighted amplitude envelope for the EXAFS contribution of Fe-Fe, Fe-Si, and Fe-O pairs. Solid lines correspond to $k^3A_{ij}(k)$ functions, and dotted lines to $kA_{ij}(k)$ functions. (**b**) Relative amplitude of the Fe-Fe/Fe-Si (solid line) and Fe-Fe/Fe-O (dotted line) contributions. (c) k^3-weighted (solid line) and *k*-weighted (dotted line) RSF for Garfield nontronite.

$$\mathrm{FT}\,[k^n\chi] = \int_{k_{\min}}^{k_{\max}} k^n \chi_{ij}(k,\theta) e^{-2ikR} dk \qquad (10)$$

Equation 9 indicates that the amplitude of the sine wave is determined by two types of parameters, namely, those which depend on k [F, λ, and exp $(-2\sigma^2k^2)$], and those which are independent of k (N, R, θ). Consequently, the k-weighting solely affects the relative importance of the first three terms. Figure 2a compares the k- and the k^3-weighted $A_{ij}(k) = F_j(k)$ exp $(-2\sigma_{ij}^2k^2)$ exp $(-2R_{ij}/\lambda(k))$ functions for the Fe-Fe, Fe-Si, and Fe-O pairs. These functions represent the amplitude envelop of the sine function (i.e., the EXAFS contribution) for the three atomic shells, Fe, Si, and O. They were calculated for R = 3 Å and σ = 0.09 Å, and $F_j(k)$ and λ(k) were generated by the FEFF 7.02 code (Rehr et al. 1991) for a nontronite cluster (Manceau et al. 1998). From Figure 2a we deduce that: (1) The wave amplitude increases with the atomic number of the backscattering atom, that is, with its number of electrons. Heavy elements are thus more easily detected than light elements, which is especially true for distant atomic shells as the wave amplitude decreases with $1/R^2$ (Eq. 9). For this reason, second- and third-nearest oxygen shells are hardly detected by powder EXAFS spectra. They may be detected, however, using polarized techniques by orienting the electric field vector in their direction (Manceau et al. 1998). (2) The shape of $k^nA_j(k)$ functions varies with j and n. For 3d atoms, these functions always have a maximum near k = 7–9 Å^{-1} regardless of n, and the amplitude drops rapidly outside of this k value range. In contrast, O and Si functions have a smoother k variation. To emphasize this difference of k variation of $A_j(k)$ as a function of j, but also to eliminate the influence of the k^n-weighting on the wave envelope, one can compare the ratios A_{Fe}/A_{Si} and A_{Fe}/A_O. The relative variations of the Fe/Si and Fe/O contributions are plotted in Figure 2b. These plots show that the contribution of Fe shells to the EXAFS spectrum, relative to O and Si, progressively increases from 3 Å^{-1} to ~8–9 Å^{-1} before reaching a plateau. Stated another way, the amplitude of EXAFS oscillations beyond ~8 Å^{-1} is dominated by the contribution of Fe atoms over that of O and Si. (3) The k^n weighting modifies the shape of $k^nA_j(k)$ functions but, as this shape varies with the nature of the atomic pair (see previous point), this k^n weighting allows reinforcement of the contrast of amplitudes among the various atomic pairs. This effect can be quantified by calculating the integral intensity of $k^nA_j(k)$ over k, as is done in the Fourier transform (Eq. 10). I$[k^nA_j(k)]$ values for Fe, Si, and O were calculated in the 3 Å^{-1} ≤ k ≤ 14 Å^{-1} interval. Relative I$[kA_j(k)]$ values for Fe, Si, and O are equal to 49, 33, and 18%, and I$[k^3A_j(k)]$ values to 56, 30, and 14%, respectively. These results show that by performing the Fourier transform on k^3, the Fe-Fe EXAFS contributions are amplified in the RSF relative to Fe-O, whereas Fe-O contributions are enhanced by the k weighting. The relative gain in intensity of the Fe contribution over that of the O contribution from the k- to k^3-weighting is given by the ratio I(k^3A_{Fe}) × I(kA_O)/I(kA_{Fe}) × I(k^3A_O), which equals 1.5. This leads us to the important conclusion that contributions of Fe shells to the RSF are magnified by 50% relative to those of O shells when the Fourier transform is performed on $k^3\chi$ instead of $k\chi$. Conversely, the contributions of O shells are amplified by 50% by using a k-weighting scheme.

These theoretical considerations are verified experimentally in Figure 2c, which compares FT$[k\chi]$ and FT$[k^3\chi]$ functions for Garfield nontronite. The first peak corresponds to the nearest Fe-O1 contribution at R = 2.01 Å, and the second derives predominantly from octahedral edge-sharing Fe-Fe pairs (Oct1) at R = 3.05 Å. Note that RSF peaks are shifted by ΔR ~–0.3 Å with respect to crystallographic values (R) because Fourier transforms are generally uncorrected from phase shift functions $\phi_{ij}(k)$ (Eq. 9), which depend on the ij pair and thus vary from one peak to another. After normalization of the y axis to the intensity of the first oxygen peaks, one notes in Figure 2c that the relative intensities of the two nearest Fe-Fe peaks are different:in FT$[k^3\chi]$ it is amplified by ~50% as predicted by theory. Two other peaks at $R + \Delta R$ = 5.0 Å and 8.8 Å, corresponding to distant Fe shells, are also amplified by the k^3 weighting.

Values for R and N_{cryst} in the nontronite samples were determined by fitting Fourier back-transformed (FT^{-1}) RSF peaks. F_O and ϕ_{Fe-O} functions were calculated experimentally from Garfield nontronite (N_O = 6, R = 2.01 Å) (Manceau et al. 1998). Functions for Fe-Fe, Fe-Si, and Fe-Al pairs were calculated *ab initio* by the FEFF 7.02 code (Rehr et al. 1991), and their validity was tested on Garfield nontronite. The absolute accuracy of N_{cryst}, as shown below, is better than 20%. Based on the comparison between X-ray diffraction and EXAFS data, the absolute accuracy on R is typically 0.02 Å.

RESULTS AND INTERPRETATION

Pre-edge spectroscopy

Pre-edge spectra are derived predominantly from 1s to 3d dipolar transitions. At the Fe K-edge this spectroscopy probes the density of 3d electronic states of Fe. Point group selection rules indicate that 3d transitions are not allowed in O_h symmetry, whereas in T_d symmetry the $1s(a_1) \rightarrow t_2$ transition is allowed. Accordingly, no pre-edge should be observed for octahedrally coordinated Fe. In fact, the intensity of the pre-edge depends on both the local symmetry and the electronic properties of the cation. It is low for common octahedral sites, but substantial for tetrahedral sites. Figure 3a shows that the oscillator strength for $^{IV}Fe^{3+}$ in $FePO_4$ is typically 10 times greater than that for $^{VI}Fe^{3+}$ in Garfield nontronite. This amplitude contrast is high and has been used to evaluate cation site occupancy in minerals (see e.g., Farges et al. 1997; Manceau et al. 1990; Manceau and Gates 1997). Figure 3a also shows that the pre-peak of sixfold coordinated Fe is split into t_{2g}- and e_g-like components with a separation of ~2 eV, whereas in tetrahedral coordination the e- and t_2-like levels are close in energy (Douglas et al. 1994), and therefore appear as a single peak.

The intensity of pre-edge spectra is about 1.5 to 3% of the main absorption edge, which indicates that Fe atoms are predominantly sixfold coordinated (Fig. 3b). The pre-edge intensity gradually increases from the Garfield to the NG-1 sample. This last sample displays a single maximum as for the $^{IV}Fe^{3+}$ reference compound. Two explanations can be proposed for this spectral evolution. The first interpretation is that some of the Fe in the clay is tetrahedral, i.e., $^{IV}Fe^{3+}$ species are present. The possible amount of tetrahedral Fe in the various samples was evaluated by linear combinations of $^{VI}Fe^{3+}$ and $^{IV}Fe^{3+}$ refer-

ence spectra (Fig 3c). Using this simulation as a calibration for the experimental spectra of the clays, the maximum amount of $^{IV}Fe^{3+}$ in nontronites PV, SWa-l, and NG-1 would be 3, 8, and 12%, respectively.

The second interpretation considers that the pre-peak intensity is not uniquely related to coordination number but also depends on the geometry of the Fe site (Manceau and Gates 1997). If a trigonal (C_{3v}) distortion is introduced at the octahedral Fe site, a portion of the formerly forbidden transitions become allowed, and the intensity of the pre-edge increases. In Garfield nontronite, the site symmetry presumably is high because the Fe atoms occupy only cis sites (M2) (Besson et al. 1983) and the octahedral sheets are almost devoid of Al ($Fe_{Oct}:\Sigma_{Oct}$ = 0.91, Table 2), which accounts for the low pre-edge intensity. The increase in pre-edge intensity from Garfield to NG-1 cannot be attributed to the presence of Fe in some trans (M1) sites (Lear and Stucki 1990), which possess a different geometry from cis (M2) sites, because this explanation is inconsistent with X-ray diffraction results (see below). Instead, the increase in intensity in the series Garfield < PV < SWa-1 correlates with the increase in octahedral Al as $Fe:\Sigma_{Oct}$ cation ratios are 0.91, 0.72, and 0.67, respectively. This explanation is plausible for these three nontronites, but not for sample NG-1 because its $Fe:\Sigma_{Oct}$ ratio equals 0.92, a value virtually identical to that of Garfield, but the intensity of its pre-edge peak is the greatest and Garfield's is the weakest in the series. As shown below, P-EXAFS results offer strong evidence for ~17 ± 3% $^{IV}Fe^{3+}$ in NG-1 and that PV and SWa-l are devoid of $^{IV}Fe^{3+}$. Consequently, the higher intensity of NG-1 pre-edge is interpreted by the presence of $^{IV}Fe^{3+}$, and the intermediate intensity of PV and SWa-1 is interpreted by a lowering of the Fe^{3+} site symmetry due to the mixing of Fe and Al/Mg atoms in octahedral sheets, and not to the presence of tetrahedral Fe.

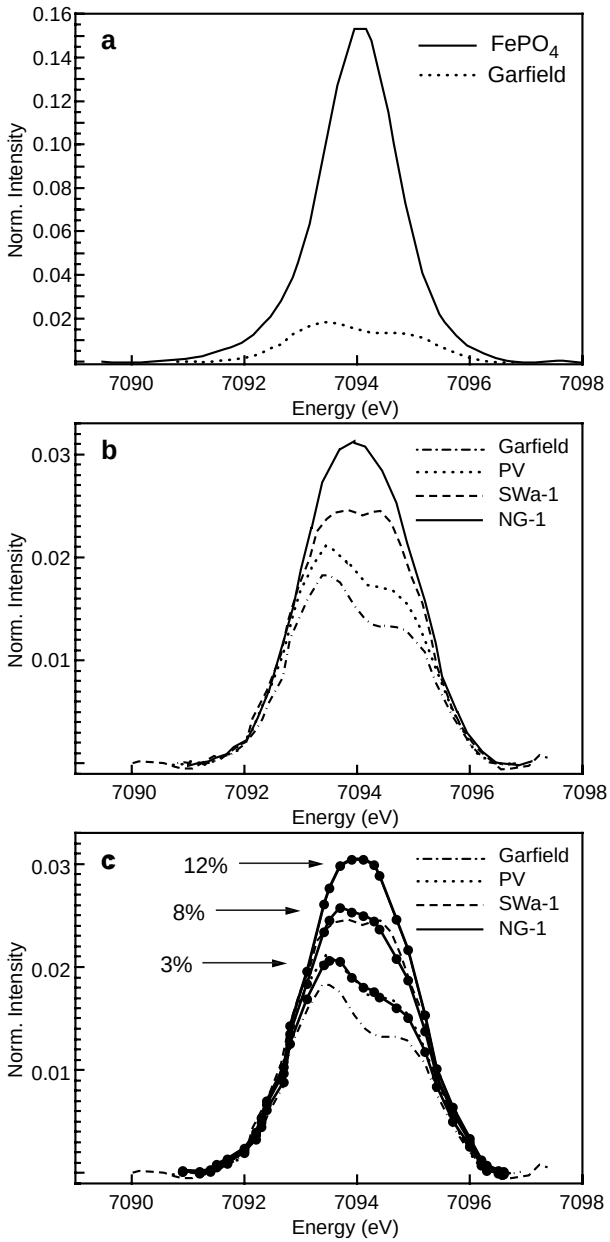

FIGURE 3. Fe K pre-edge spectra for Garfield nontronite ($^{VI}Fe^{3+}$) and $FePO_4$ ($^{IV}Fe^{3+}$) reference material (**a**), for nontronite samples (**b**), and for linear combinations of $^{VI}Fe^{3+}$ and $^{IV}Fe^{3+}$ references materials (**c**).

Powder XRD

XRD patterns (Fig. 4) display only basal reflections (001, 002, and 003) and two-dimensional *hk* bands (02-11, 20-13, 04-22, 15-24-31, and 06-33) as a consequence of the turbostratic stacking of layers (Brindley and Brown 1980). The most significant differences observed were in the 06-33 reflection, the position of which increases from 1.509 Å in SWa-l, to 1.514 Å for

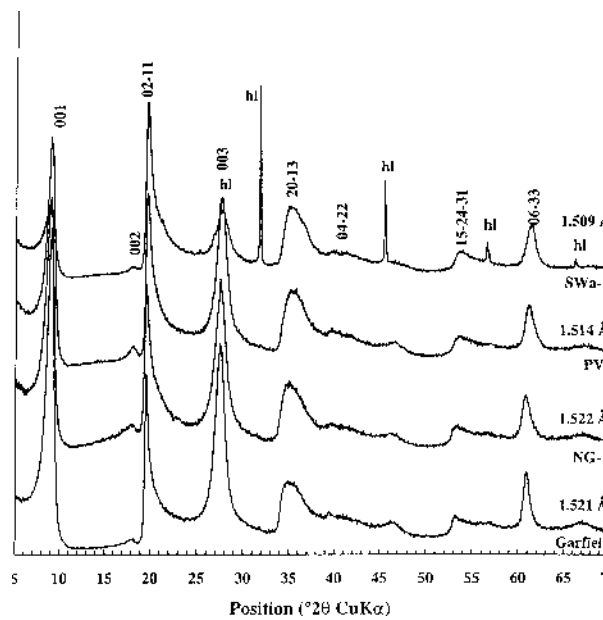

FIGURE 4. Experimental powder X-ray diffraction patterns of the four nontronite samples recorded in vacuum [*d*(003) ~3.25 Å]. hl indicates halite impurity in SWa-1 sample. Diffraction maxima are indexed, and *d*(060) is indicated for each sample.

PV, and to 1.521–1.522 Å for both NG-1 and Garfield. Except for NG-1, this follows the Fe_{Oct}:Σ_{Oct} ratio (Radoslovich 1962), which increases in the order SWa-1 (0.67) < PV (0.72) < Garfield (0.91). This ratio equals 0.77 in NG-1 when 17% of Fe^{3+} are placed in tetrahedral sites (Table 2) and its relatively high *b* value (Table 3) can be explained by the larger lateral size of the tetrahedral sheet as a result of the $^{IV}Fe^{3+}$ for Si substitution.

As mentioned above, oblique texture electron diffraction showed that dioctahedral Fe^{3+}-rich clay minerals are trans-vacant, but this technique is not sensitive enough to exclude completely the presence of some Fe^{3+} in trans sites. For this purpose, the intensity of the 02-11 and 20-13 bands were calculated for different site occupancies and compared to experimental patterns. Indeed, Drits et al. (1984) showed from the calculation of 02*l*, 11*l*, 13*l*, and 20*l* lines that the intensity of the 02-11 band for dioctahedral Al-rich clays is constant if their layers are either tv or cv, or if tv and cv layers are interstratified, especially for pure turbostratic layer stacking. If octahedral cations are randomly distributed over cis and trans sites the intensity of the 02-11 band is instead strongly reduced. Further, the intensity of the 20-13 band is independent of the distribution of octahedral cations, and its intensity can be used as an internal standard for normalizing the intensity of the calcu-

Table 3. Unit-cell parameters derived from XRD for dehydrated samples ($P = 10^{-6}$ atm)

	$c^* = 3\ d(003)$ (Å)	$b = 6\ d(060)$ (Å)	$a = b/\sqrt{3}$ (Å)
Garfield	9.73	9.13	5.28
PV	9.69	9.08	5.24
SWa-1	9.67	9.06	5.23
NG-1	9.72	9.13	5.27

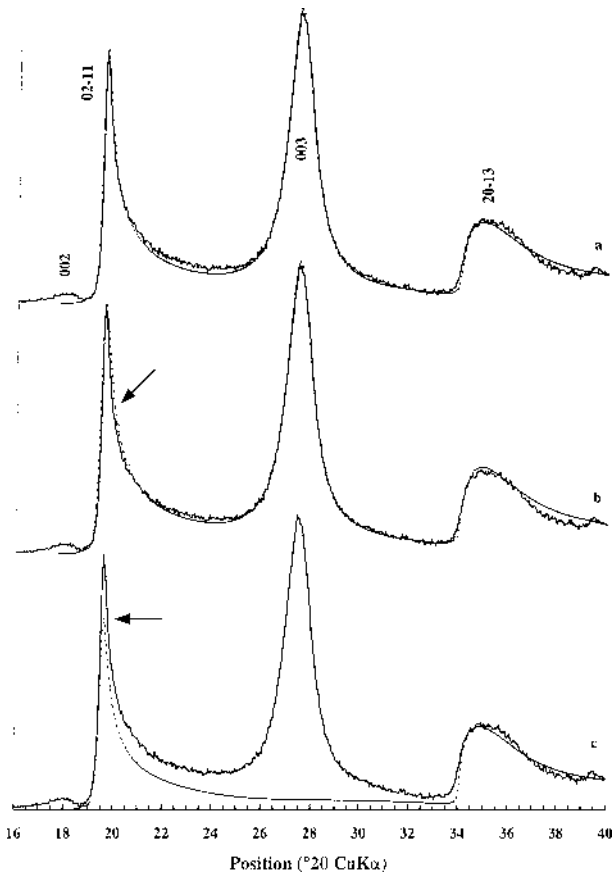

FIGURE 5. Comparison between experimental and calculated XRD patterns. (**a**) Optimum fit obtained for Garfield nontronite obtained by assuming 100% of trans-vacant sites. (**b**) XRD pattern for Garfield nontronite using a 1:4 ratio, instead of a 5:6 ratio in the optimum case, between CSDs having 200 Å and 100 Å radii, respectively. (c) XRD pattern calculated for Garfield nontronite with 10% of octahedral cations occupying trans sites. Calculations used Tables 2–4. In Figures 5a and 5c the ratio between CSDs having 200 Å and 100 Å radii is 5:6.

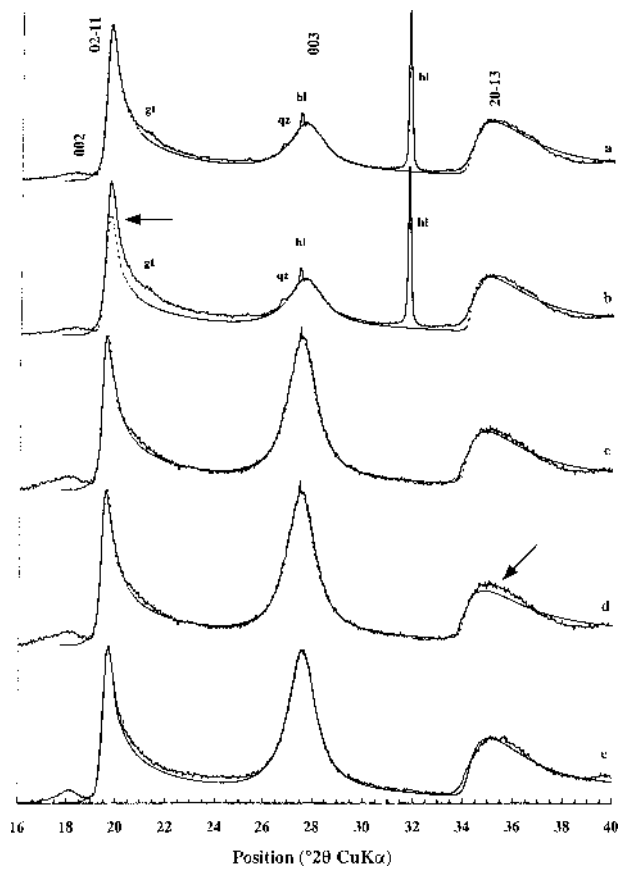

FIGURE 6. Comparison between experimental and calculated XRD patterns. (**a**) Optimum fit for SWa-1 nontronite obtained by assuming 100% of trans-vacant sites. (**b**) XRD pattern for SWa-1 with 10% of octahedral cations occupying trans sites. (**c**) Optimum fit for NG-1 nontronite obtained by assuming 100% of trans-vacant sites. (**d**) XRD pattern calculated for NG-1 with all ^{IV}Fe replaced by ^{IV}Al. (**e**) Optimum fit for PV obtained by assuming 100% of trans-vacant sites. Calculations used Table 2 (except d), 3 and 4. The ratios between CSDs having 200 Å and 100 Å radii were 1:8, 1:6, and 1:10 for SWa-1, NG-1, and PV, respectively. hl, gt, qz indicate halite, goethite, and quartz impurities, respectively, in the SWa-1 sample.

TABLE 4. Atomic coordinates in the asymmetric layer unit cell

	x	*y*	*Z*
O positions	0.630	0.688	0.613
	0.640	0.500	0.822
	0.375	0.736	0.845
	0.003	0.313	0.387
	–0.030	0.500	0.179
	0.260	0.740	0.156
	0.683	0.000	0.611
	–0.056	0.000	0.389
Tet. Cations	0.630	0.329	0.780
	0.000	0.329	0.220
Cis site	0.316	0.333	0.500
Trans site	0.316	0.000	0.500
Interlayer Na	0.646	0.000	0.892
	0.000	0.000	0.108

Notes: Atomic coordinates were calculated from the regression analysis of dioctahedral micas (Smoliar-Zviagina 1993). Coordinates are given in fraction of unit cell parameters (Table 3), for a *c*2/*m* layer symmetry and an orthogonal lattice since β is undefined due to the turbostratic layer stack. These were used to calculate the distribution of intensity of the 02-11 and 20-13 reflections for all nontronite samples.

lated XRD pattern. Consequently, the intensity ration of the 02-11 and the 20-13 bands is sensitive to the distribution of octahedral cations between trans and cis sites within the same octahedral sheet, and were used to detetect small amounts of M1 cations in predominantly tv layers.

Simulations of the 02-11 and 20-13 bands and 003 reflection are shown in Figures 5 and 6. Structure factors were calculated from structural formulae (Table 2), and atomic coordinates obtained from Smoliar-Zvyagina (1993, Table 4). Simulations showed that small variations of atomic coordinates do not significantly influence intensities of the 02-11 and 20-13 bands and, accordingly, the same atomic coordinates were used for all samples (Table 4). To obtain realistic distances of 2.40–2.50 Å between interlayer Na and O atoms defining the hexagonal cavity, interlayer Na was shifted by 1.05 Å from the middle of the interlayer space in direction of the layer, and this displacement proved to be critical for proper fitting of the 20-13 band. Coherent scattering domains (CSDs) were assumed to have a disk-like shape of 100 Å and 200 Å radii. Their relative proportions were adjusted by fitting the profile of the 02-11 band, taking into account the contribution from the 003 diffraction line as a Lorentzian-shaped curve.

Optimal fits were obtained by assuming 100% trans-vacant octahedral sites in the four nontronite samples (Figs. 5a, 6a, 6c, and 6e). The sensitivity of the method for determining the distribution of cations over cis and trans sites within the same octahedral sheet was evaluated by increasing progressively the trans site occupancy in a layer initially trans-vacant. Figures 5c and 6b compare the experimental XRD patterns for Garfield and SWa-1 to that obtained when 10% of total octahedral cations are present in trans sites. Here, 45% of octahedral cations are present in each of the two symmetrically independent cis sites, each having a 90% occupancy probability. Assumption of this small amount of Fe in trans sites dramatically decreased the intensity of the 02-11 band in the calculation, leading to the conclusion that the octahedral occupancy of trans sites, if present, is certainly less than 5% of total octahedral cations in the four nontronite samples studied.

The small discrepancy observed in Figure 6a between experimental and calculated 02-11 profiles for SWa-1 in the 21 °2θ Cu*K*α region is due to the presence of a small amount of fine-grained goethite. A similar effect may exist also in the NG-1 sample. For this sample, the sensitivity of the 02-11 to 20-13 intensity ratio to the presence of $^{IV}Fe^{3+}$ was also tested. XRD patterns calculated for a tv NG-1 model with 17% $^{IV}Fe^{3+}$ (Fig. 6c) and with only Al for Si tetrahedral substitution (Fig. 6d) are almost identical, indicating that this ratio has very low sensitivity to the presence of fourfold Fe. Therefore, it can only be used to determine the site occupancy of octahedral cations in turbostratic layer silicates.

Quantitative texture analysis

The typical evolution of the X-ray diffraction pattern for PV as a function of the tilt angle ρ up to ρ = 70° (Fig. 7) indicates that a high degree of crystallite alignment exists (strong texture), with the <001>* direction perpendicular to the film plane. Qualitatively, the FWHM of the dispersion appears to be 30–35° and, even without normalization at this stage of analysis, it is greater than for Garfield (19.8°, Manceau et al. 1998). The 001 reflection is the most intense, but was not retained for the normalization because at this low Bragg angle of irradiation the surface varies substantially with ρ. The experimental (004) pole figures and radial distribution of *c** in (Fig. 8) show that the Garfield nontronite has the greatest parallel orientation, with a pole density calculated in *multiples of a random distribution*, (mrd), of 37.1 at maximum and a FWHM of 19.6°. SWa-1 has the least parallel orientation, with 14.3 mrd of distribution density at maximum and a FWHM of 38.5°. Also for this sample ρ_1 = 38.2°, which means that densities higher than for a random powder (1 mrd) are present at angles larger than the EXAFS's magic angle of 35.3°. PV and NG-1 samples have intermediate texture strengths, with maximum

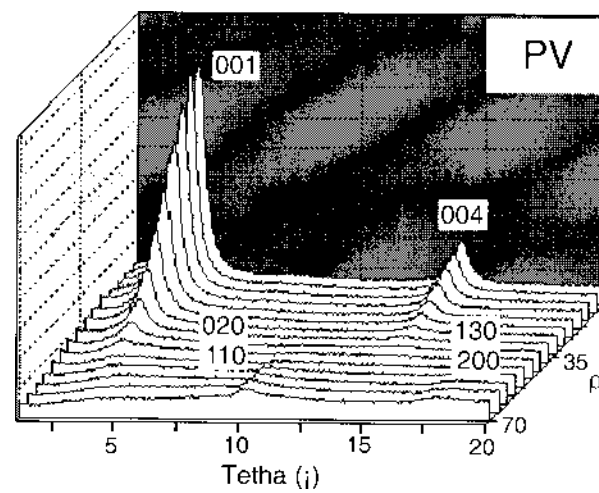

FIGURE 7. Variation of diffraction pattern as a function of the tilt angle, ρ, for a self-supporting film (PV). The severe decrease of 001 and 004 lines with ρ indicates a strong texture. Net intensities were used for texture calculations. Patterns were recorded in air [*d*(004) = 3.1 Å].

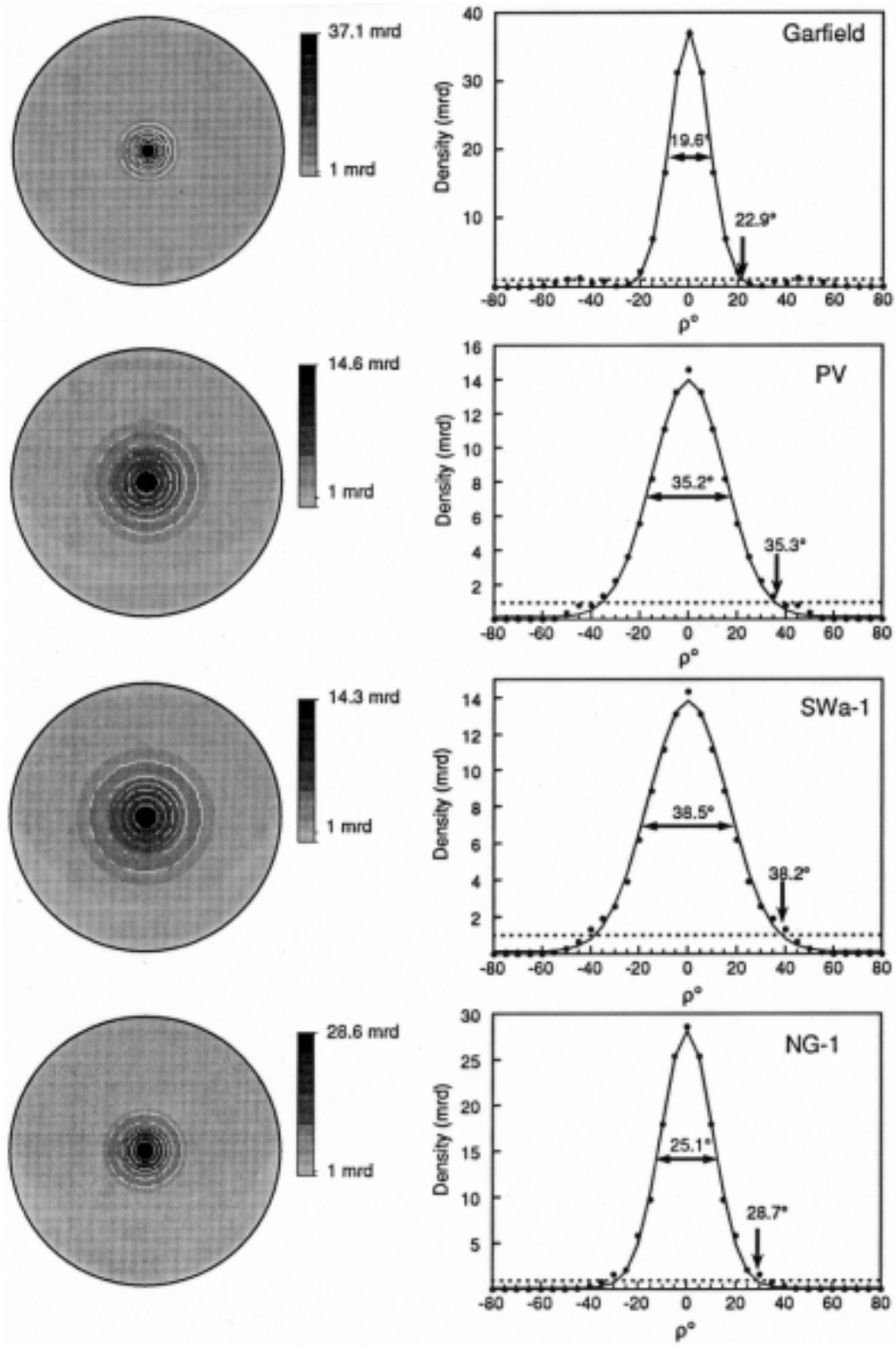

FIGURE 8. Pole figure for the 004 reflection **(left)** and corresponding radial distribution densities of the dispersion of clay platelets off the film plane for the four samples **(right)**. The strong maximum of intensity at the center of the (004) figure quantifies the <001>* fiber texture (ρ = 0°). The 1 mrd density (perfectly random powder) is represented by a horizontal dashed line. Linear density scale and equal area projection are used for the pole figures.

densities close to 14.6 mrd (FWHM = 35.2°) and 28.6 mrd (FWHM = 25.1°), respectively.

Textural analysis shows that dispersion of the individual crystallite c^* axes is relatively low. The highest dispersion from perfect alignment observed for SWa-1 should diminish slightly the angular dependence of its P-EXAFS spectra. The difference between N_{eff} estimated from the crystallographic structure assuming an idealized texture (Eq. 6), and the real value experienced by P-EXAFS (N_{exafs}), was calculated by Manceau et al. (1998b) for the case of a continuous inclination of the c^* axis symmetrically around the film normal. These calculations showed that for a distribution of $\Delta\rho = \pm 20°$, $(N_{eff}–N_{exafs})/N_{eff}$ is equal to 11% at $\alpha = 90°$ for the Oct-Tet1 pair, and to 4% at $\alpha = 0°$ for the Oct-Oct1 pair. Consequently, the dispersion of crystallites in our nontronite films should have little effect on N_{eff} and is initially neglected in a first approximation.

P-EXAFS

***k*³-weighted EXAFS spectra**. The signal to noise ratio of the spectra is high over the whole k range, allowing visualization of their angular dependence (Fig. 9). Well-defined isosbestic points are present at values of k for which $k^3\chi(k)$ is independent of α. The large dependence on polarization is consistent with the successful preparation of highly oriented clay films. The $k^3\chi(k,\alpha = 90°)$ spectrum was calculated by the linearization and extrapolation procedure described above. Regression coefficients as a function of k (Fig. 10) show that r^2 is generally greater than 0.9 for $k < 10$ Å^{-1}. In this wavevector range, points with lower r^2 values correspond precisely to isosbestic points (Manceau et al. 1998), and the regression procedure obviously has no statistical significance wherever $k^3\chi$ is independent of α. Values for r^2 are more dispersed above 11–12 Å^{-1} as a result of the progressive signal damping, and concomitant increase of noise. However, except for the isosbestic points, r^2 remains generally greater than ~0.8 over the entire k span for Garfield nontronite, PV, and NG-1. The situation is worse for SWa-l, for which the correlation diminishes beyond k = 9–10 Å^{-1}. All nontronite spectra have similar signal/noise ratios (Fig. 9) and, consequently, the degradation of r^2 observed for SWa-l cannot be explained by increased noise at higher k. Instead, SWa-l has a markedly lower angular variation of $k^3\chi$ above 8.5 Å^{-1} than the other three nontronite samples (Fig. 9). This is particularly noticeable in the two oscillations peaking at 10.2 and 10.6 Å^{-1}, which have a very weak polarization dependence. As for isosbestic points,

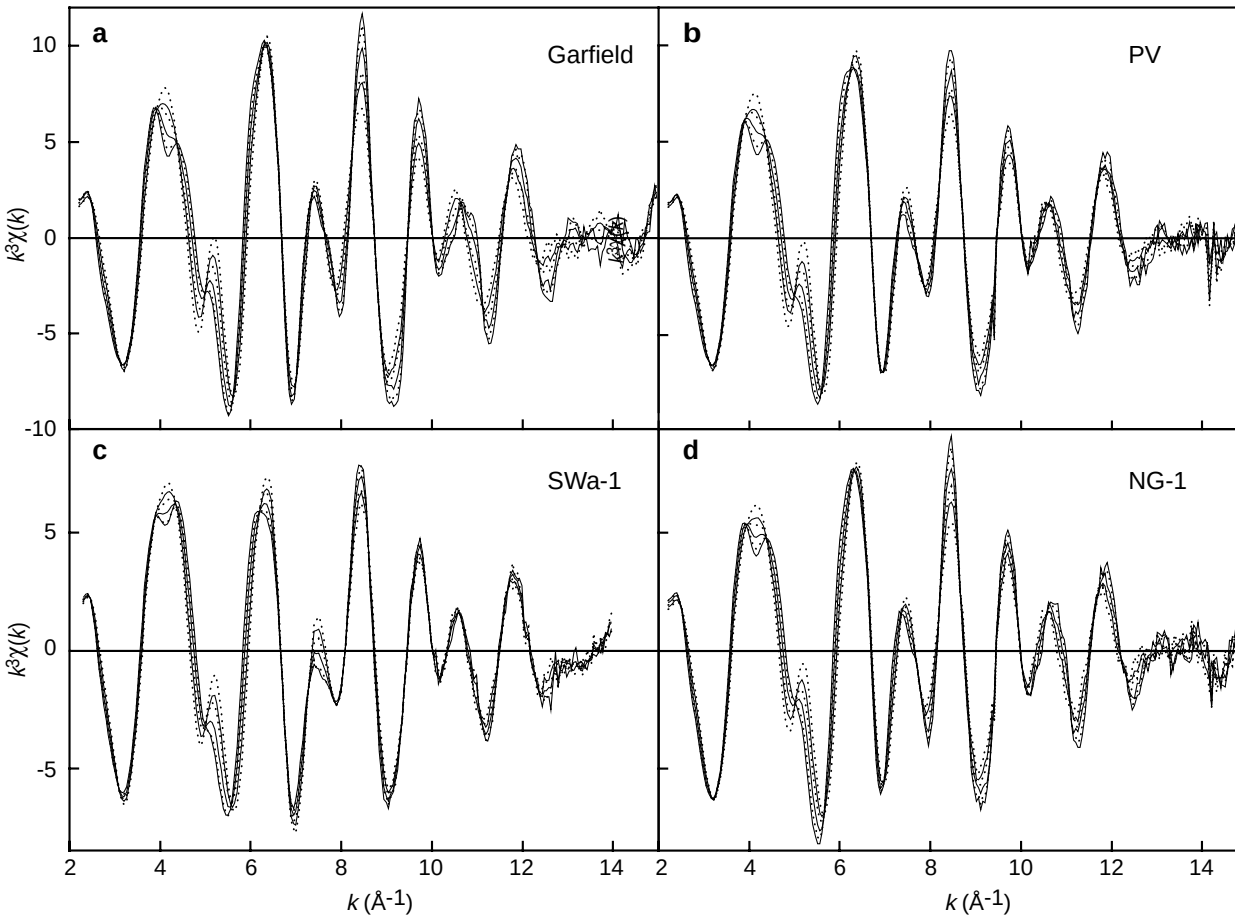

FIGURE 9. k^3-weighted Fe K-edge P-EXAFS spectra for nontronites at α angles of 0°, 20°, 35°, 50°, 60°, and 90°. The 90° spectrum was obtained by regression of the experimental amplitude (see text). The amplitude of k^3 decreases with increasing α at 8.5 Å^{-1}, and increases with α at 4 Å^{-1}. Note the presence of isosbestic points where $k^3\chi$(k,d) is independent of **d**.

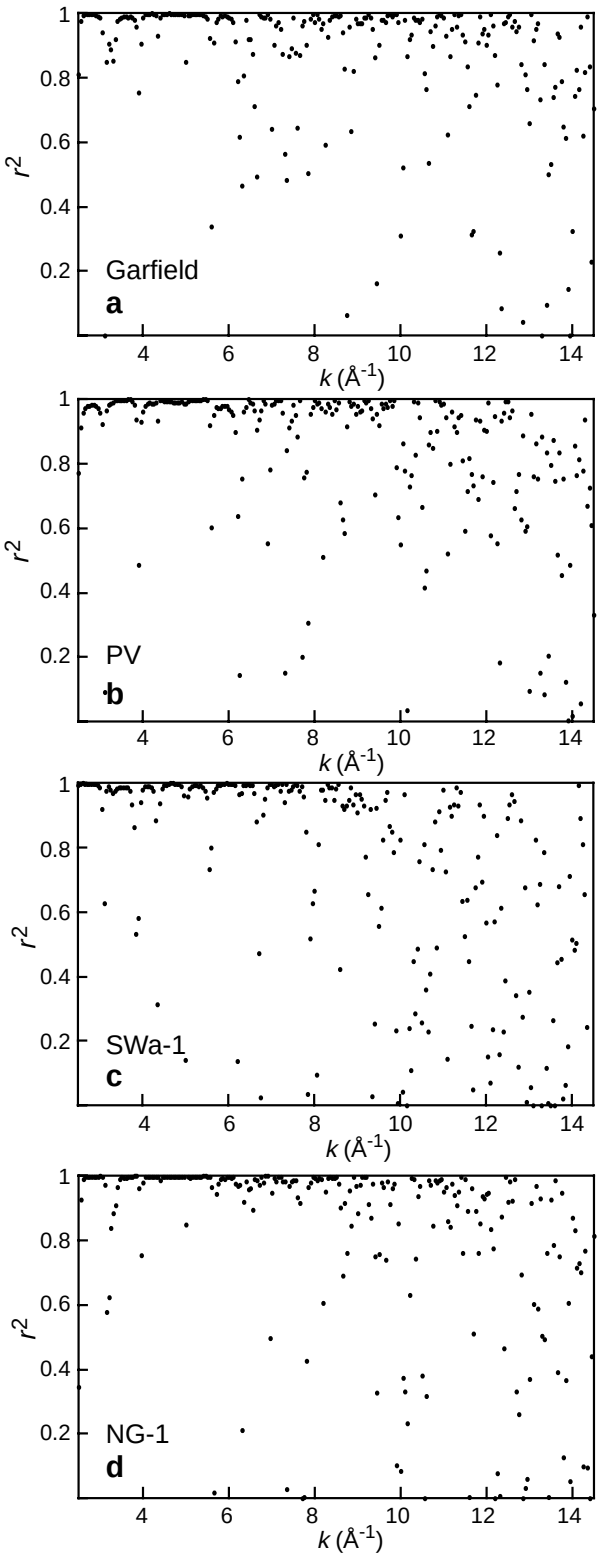

FIGURE 10. r^2 (regression coefficient of determination) as a function of k.

this lower angular dependence of $k^3\chi$ causes a decrease of r^2. This spectral feature is unlikely to result from the lower parallel orientation of platelets in the film plane because sample PV, which has a similar texture strength (FWHM = 38.5° for SWa-1 but 35.2° for PV), exhibits a large angular variation at high k, and also because the reduction of the polarization dependence should be observed over the whole k span. Thus the reduction of the spectral anisotropy in this particular wavevector range is probably of structural origin.

The accuracy of the extrapolations was also assessed visually by comparing experimental EXAFS spectra to those recalculated ($k^3\chi_{cal}$) from linear regression lines at given α angles. Manceau et al. (1998) showed that experimental and recalculated $k^3\chi(k,\alpha = 35°)$ for Garfield nontronite deviate by only a few percent. This difference has been quantified in Table 5 by calculating the profile reliability factor (R_p) between $k^3\chi_{exp}$ and $k^3\chi_{cal}$ for each α value. $< R_p >$, averaged over the 5 experimental angles, equals 0.8×10^{-3} (Garfield), 1.5×10^{-3} (PV), 1.8×10^{-3} (SWa-l), and 1.3×10^{-3} (NG-1). In conclusion, this analysis engenders confidence in the calculation of $k^3\chi(k,\alpha = 90°)$.

Radial structure functions. RSFs obtained by Fourier transforming k^3-weighted P-EXAFS spectra are shown in Figure 11. The structural nature of the RSF peaks was determined by Manceau et al. (1998) in the case of Garfield nontronite. This assignment can be extended to the three other nontronite samples because they have very similar RSF shapes. Peak A corresponds to the O,OH ligand shell (O1, Fig. 1b, Table 1), and its angular dependence has been shown to be directly connected to the symmetry of the coordination polyhedron, and specifically to the flattening angle in the case of octahedral coordination (Manceau et al. 1998). Peak B results from the contributions of the nearest Fe,Al,Mg shell (Oct1) located in the octahedral sheet, and of the nearest tetrahedral Si,Al shell (Tet1) located apart from the octahedral sheet (Fig. 1). In the in-plane orientation, the contribution from Oct1 atoms at the crystallographic R distance of ~3.05 Å is enhanced ($\beta_{oct1} = 90°$), and peak B points to the apparent distance of $R + \Delta R = 2.8$ Å. In the out-of-plane orientation, the contribution from the octahedral layer is canceled as $\beta_{Oct1} = 90°$, and that of the Tet1 shell at R ~3.28 Å maximized (β_{Tet1} ~32°, see theoretical section). Accordingly, peak B gradually shifts from $R + \Delta R = 2.8$ Å to 2.9 Å with increasing α. Peaks D and E predominantly originate from the next-nearest tetrahedral (Tet2) and octahedral (Oct2) shells (Fig. 1b, Table 1). Another peak, (B1 in Fig. 12a), is observed for $\alpha = 0°$ when the Fourier transform is performed on $k\chi(k)$ instead of $k^3\chi(k)$. This peak corresponds to the next-nearest O,OH shell (O2) (Manceau et al. 1998), and its contribution is logically reinforced by the k weighting as explained

TABLE 5. Profile reliability factor (R_p) between experimental and recalculated P-EXAFS spectra

	$\alpha = 0°$	$\alpha = 20°$	$\alpha = 35°$	$\alpha = 50°$	$\alpha = 60°$	$<R_p>$
Garfield	$0.8\ 10^{-3}$	$0.9\ 10^{-3}$	$0.9\ 10^{-3}$	$0.6\ 10^{-3}$	$0.6\ 10^{-3}$	$0.8\ 10^{-3}$
PV	$0.8\ 10^{-3}$	$1.5\ 10^{-3}$	$2.6\ 10^{-3}$	$1.3\ 10^{-3}$	$1.3\ 10^{-3}$	$1.5\ 10^{-3}$
SWa-1	$0.9\ 10^{-3}$	$1.8\ 10^{-3}$	$2.7\ 10^{-3}$	$1.9\ 10^{-3}$	$1.6\ 10^{-3}$	$1.8\ 10^{-3}$
NG-1	$0.5\ 10^{-3}$	$1.3\ 10^{-3}$	$1.8\ 10^{-3}$	$1.9\ 10^{-3}$	$1.2\ 10^{-3}$	$1.3\ 10^{-3}$

Notes: R_p is the figure of merit for the spectral fitting, $R_p = \Sigma\ (k^3\chi_{exp} - k^3\chi_{th})^2 / \Sigma\ (k^3\chi_{exp})^2$.

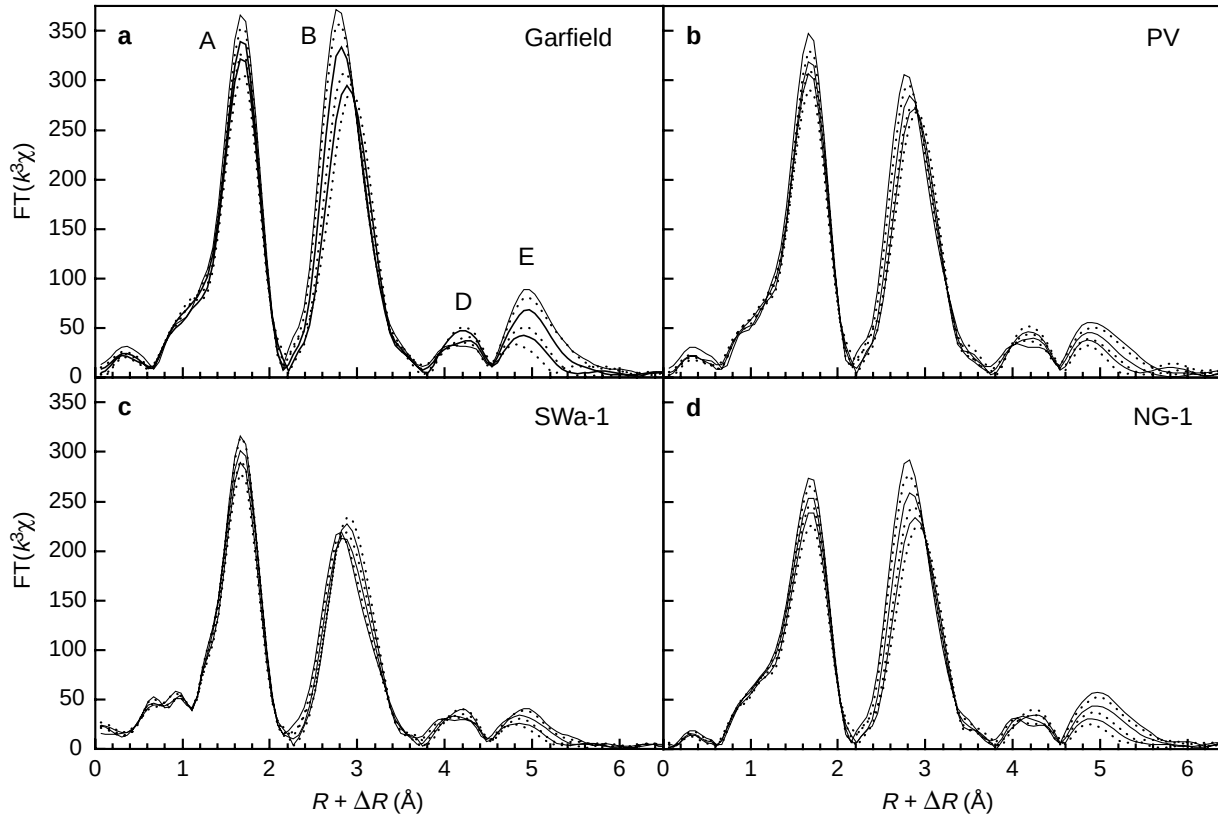

FIGURE 11. k^3-weighted Fe K-edge polarized RSFs for nontronites at α angles of 0°, 20°, 35°, 50°, 60°, and 90°. The amplitude of peaks A, B, and E decreases with increasing α. Thus solid lines correspond, in decreasing amplitude, to α = 0°, 35°, and 60°, and dotted lines to α = 20°, 50°, and 90°.

above. Hence, peak B is the sum of three contributions (Oct1, Tet1, O2) that are unresolved in powder EXAFS spectra. These three contributions can be quite completely filtered by polarized experiments, see below.

The four RSFs have different amplitudes (Figs. 11, 12b, and 12c). The magnitude of peak A decreases from Garfield nontronite to PV, SWa-l, and NG-1 regardless of α, which indicates a decrease of coherence of Fe-(O,OH) distances along this sample series. This result is consistent with pre-edge spectroscopy (Fig. 3) which indicated that the average symmetry of Fe sites decreases in the same order. The amplitude of peak B for PV, SWa-l, and NG-1 at α = 90° is lower than that of Garfield nontronite. The difference observed for NG-1 at α = 90° comes from tetrahedral Fe^{3+} atoms which have no $(Si,Al)_{Tet1}$ neighbors but Fe_{Oct1} neighbors ($^{IV}Fe^{3+}$-$^{VI}Fe^{3+}$ pairs) whose EXAFS contribution subtracts to the predominant $^{VI}Fe^{3+}$-$(Si,Al)_{Tet1}$ signal due to the π phase shift between Fe and Si,Al backscatterer (Manceau 1990). The lowering of the Fe-$(Si,Al)_{Tet1}$ contribution in PV and SWa-1 partly results from the lower textural order of individual particles in these two film samples. The decrease in amplitude of their second RSF peaks equals 7% and 19%, which is in reasonably good agreement with the reduction factor estimated from the texture analysis [$(N_{eff}-N_{exafs})/N_{eff}$ = 11%)].

At α = 0°, PV and SWa-l have also a less intense peak B than Garfield nontronite, but the drop in amplitude amounts to 18% and 41% and is much too high to be accounted for by texture effects. As discussed above and by Manceau et al. (1998), Oct1 contributions are appreciably less sensitive to disorientation than Tet1 contributions and, consequently, this factor fails to explain the observed reduction of amplitude in the parallel orientation. Instead, this reduction results from a modification in the cationic environment of Fe in the octahedral sheet. Given that the concentration of $(Al,Mg)_{Oct}$ increases from Garfield (0.36) to PV (1.12) and to SWa-l (1.31; Table 2), and that electronic waves backscattered by Fe and Al,Mg are out-of-phase (Manceau 1990), this spectral evolution suggests an increase in the number of Fe-$(Al,Mg)_{Oct}$ pairs along this sample series. The RSF peak B for NG-1 is difficult to interpret unambiguously because it contains several individual contributions from $^{IV}Fe^{3+}$ and $^{VI}Fe^{3+}$ centers, i.e., $^{IV}Fe^{3+}$-Si, $^{VI}Fe^{3+}$-$^{VI}Fe^{3+}$, $^{VI}Fe^{3+}$-Al. In the following two sections the different atomic shell contributions will be analyzed successively to explain more quantitatively the reasons for the spectral differences among the various samples observed on the modulus of the Fourier transforms (RSFs).

First oxygen shell analysis. The contributions from the first O shells were analyzed quantitatively by Fourier backtransforming first RSF peaks of powder (Garfield, SWa-1, NG-1) or polarized (PV) EXAFS spectra in the [1.2–2.2 Å] R+

ΔR range. Two different situations were observed, and are displayed in Figures 13a to 13c. Figures 13a, and b show that Fe-O1 contributions for Garfield, PV, and SWa-l are *precisely* in phase from k = 3 Å^{-1} to 16.5 Å^{-1}. This indicates that the three samples have the same $<R_{Fe\text{-}O1}>$ distance of 2.01 Å, which is characteristic of sixfold coordinated Fe^{3+}. A good spectral fit (R_p = 1–2 × 10^{-3}) was obtained by assuming 5.8 (PV) and 5.6 (SWa-l) O atoms at 2.01 Å (Table 6). The decrease of N_O from 6.0 in Garfield to 5.6 in SWa-l explains the differences in wave amplitudes observed experimentally in Figure 13b. This diminution does not reflect a real loss of O neighbors, but means that individual Fe-O distances are significantly more dispersed in the aluminous nontronite, which is consistent with pre-edge results.

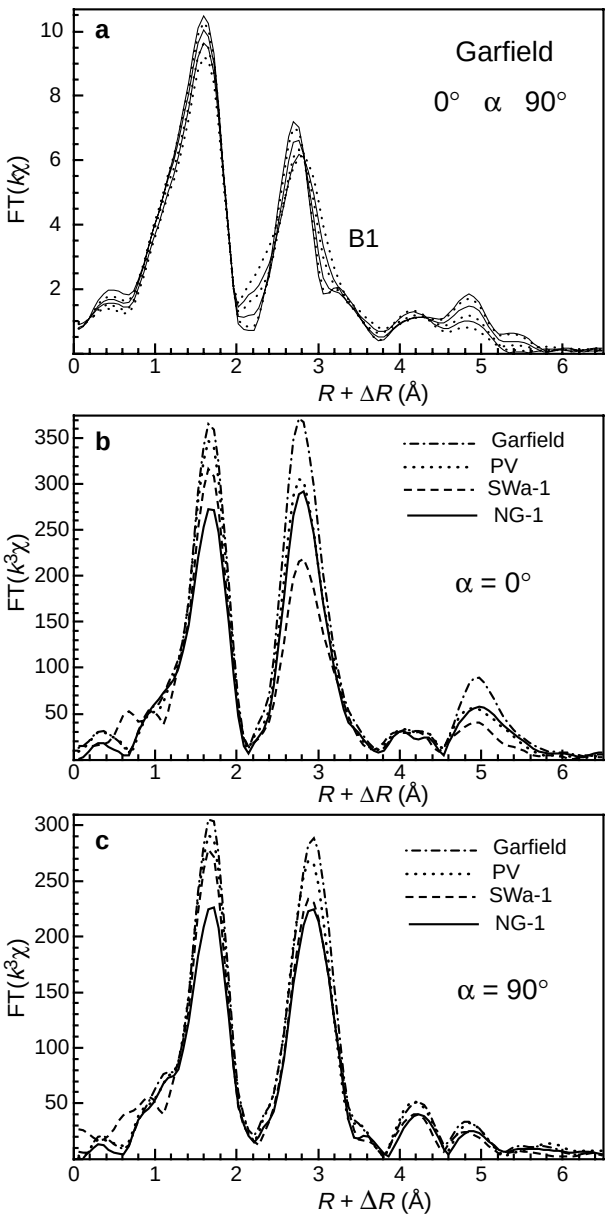

FIGURE 12. *k*-weighted Fe K-edge polarized RSFs for Garfield nontronite.

The second situation observed involved only sample NG-1, which possesses a singular wave frequency (Fig. 13c). Compared to Garfield, its wave is slightly shifted to the right at k = 4 Å^{-1}, and clearly shifted to the left for k > 13 Å^{-1}. This phase mismatch indicates the presence of at least two discrete Fe-O shells, and the assumption of a single structural distance (one-shell fit) provided only an approximate fit to this spectrum, with a figure of merit (R_p) as poor as 1.1 × 10^{-2} (Table 6). The peculiar wave frequency of NG-1 could be accounted for by assuming the presence of tetrahedrally coordinated Fe^{3+}. Figure 13d compares the theoretical $k^3\chi_{Fe\text{-}O1}$ EXAFS contributions obtained for an octahedral coordination (6 O at 2.01 Å) and a tetrahedral coordination (4 O at 1.85 Å, Arnod 1986). One can observe that the two waves are precisely out-of-phase for 8.5 Å^{-1} < k < 10.5 Å^{-1}, and shifted in opposite directions outside of this interval. Evidently, the admixture of a small fraction of $^{IV}Fe^{3+}$ with the predominant $^{VI}Fe^{3+}$ species results in the wave frequency behavior observed experimentally for NG-1 (Fig. 13c). The best spectral fit for NG-1 was obtained by assuming 5.0 O at 2.01 Å and 0.7 O at 1.85 Å (R_p = 2 × 10^{-3}), which corresponds to ~17% of tetrahedrally coordinated Fe (Fig. 14a). The accuracy of this percentage was evaluated by following the variation of R_p as a function of the amount of $^{IV}Fe^{3+}$. The quality of the fits for $^{IV}Fe^{3+}$ = 9 and 25% (Figs. 14b and 14c) are particularly poor (R_p = 1.1 × 10^{-2}), and the interval of possible $^{IV}Fe^{3+}$ values should be narrower. The range of possible $^{IV}Fe^{3+}$ values was estimated as $2R_p$ (4 × 10^{-3}), which corresponds to a minimum of 14% and a maximum of 20%.

Analysis of the first coordination shell of Fe in NG-1 and SWa-l explains the variations of peak intensities observed in pre-edge spectroscopy (Fig. 3b) and on RSFs (Fig. 12b), and which reflected a loss of structural order in these two samples as compared to Garfield. In NG-1 the main source of disorder is clearly the mixing of $^{IV}Fe^{3+}$ and $^{VI}Fe^{3+}$ species. The lack of an inversion center in FeO_4 tetrahedra is responsible for the increase of the pre-edge intensity, whereas the difference of phase between the ^{VI}Fe-O and ^{IV}Fe-O contributions (Fig. 13d) lowers the amplitude of the EXAFS signal and, therefore, of the first RSF peak (Figs. 12b and 12c). In SWa-l Fe atoms are uniquely sixfold coordinated, but Fe-O distances are more dispersed than in the two Fe-rich nontronites (PV and Garfield), as attested by the reduction in amplitude of $k^3\chi_{Fe\text{-}O1}$ for SWa-l (Fig. 13b). The distribution of the ^{VI}Fe-O distances in SWa-l may be attributed to the presence of two types of Fe-coordinated O atoms, those

TABLE 6. EXAFS parameters for Fe-O pairs

Sample	Shell	R (Å)	N_O	$\Delta\sigma$ (Å)	R_p
PV	1	2.01	5.8	0.00	0.002
SWa-1	1	2.01	5.6	0.00	0.001
NG-1	1	2.00	5.4	0.01	0.011
	2	2.01	5.0	0.00	0.002
		1.85	0.7	0.00	

Notes: Fits of EXAFS spectra recorded at α = 35° using experimental amplitude and phase shift functions derived from Garfield nontronite. Δs is the difference in the Debye-Waller factor between the sample and the Garfield nontronite reference. Shell: number of fitting shells. For all fits the variation of threshold energy for the photoelectron (ΔE) was fixed to 0.0 eV as for the reference. R_p: Figure of merit for the spectral fitting.

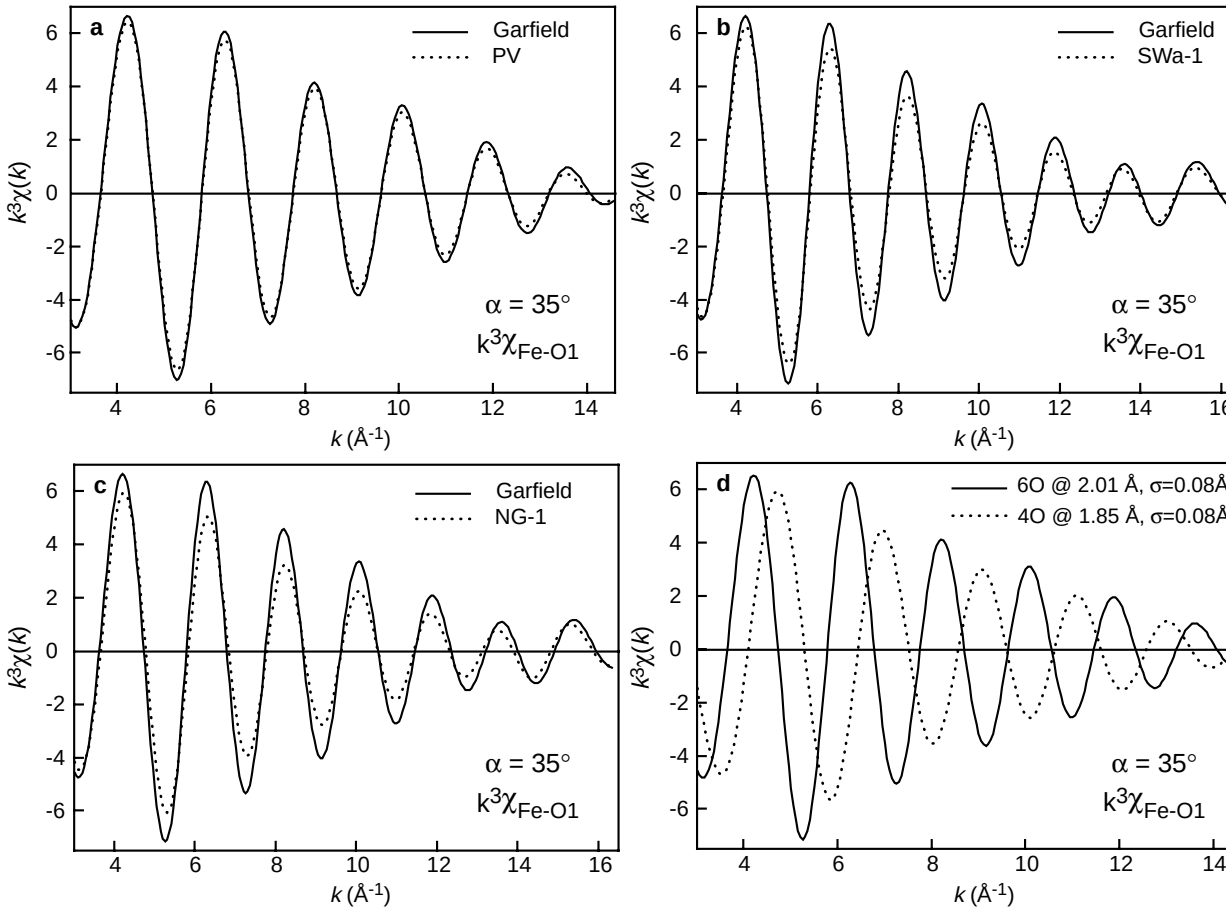

FIGURE 13. Fourier filtered Fe-O contributions to EXAFS. (**a**), (**b**), (**c**) Comparison of experimental k^3 $_{Fe\text{-}O1}$ spectra for the various nontronite samples. (**d**) k^3 $_{Fe\text{-}O1}$ for $^{VI}Fe^{3+}$ and $^{IV}Fe^{3+}$ species.

shared by two nearest Fe (Fe-O-Fe bond) and those shared by one Fe and one Al (Fe-O-Al bond) (Fig. 1b). This larger spread of the Fe-O distances in SWa-l is believed to be responsible for the increase in the pre-edge intensity (Fig. 3b).

First cation shell analysis. The second RSF peaks of phyllosilicates contain information on the distribution of cations in the octahedral sheet of layer silicates (Manceau 1990). This information is difficult to extract precisely from powder EXAFS spectra because the $\chi_{Fe\text{-}Oct1}$, $\chi_{Fe\text{-}Tet1}$, and $\chi_{Fe\text{-}O2}$ functions interfere (see "Theory"). In polarized experiments, $\chi_{Fe\text{-}Tet1}$ is obtained from the perpendicular measurement [$\chi(\alpha = 90°)$], and its in-plane contribution can be subtracted from $\chi(\alpha = 0°)$. At $\alpha = 0°$, the amplitude of the Fe-Tet1 shell is reduced to 20% of its amplitude at $\alpha = 90°$ (see, "Theory"), and this reduction factor was used to subtract the contribution of the tetrahedral sheet in the parallel orientation prior to the least-squares spectral fitting. In contrast to Tet1, the contribution of the O2 shell cannot be eliminated, so it was minimized by using *k*-weighting during the Fourier transform. The result in Figure 15a compares FT[$k\chi(\alpha = 0°)$] for Garfield nontronite to that obtained after subtracting the Tet1 contribution. Elimination of the tetrahedral contribution associated with the *k* weighting, (Fig. 15b) results in a better separation of the Fe-Oct1 and Fe-O2 components, simply because the Tet1 shell lies at a distance intermediate to the other two (Table 1, Fig. 12a). The Fe-Oct1 and Fe-O2 components are now fairly well separated for all samples, the best peak separation being observed for SWa-l. This analysis demonstrates the improved discrimination between contributions of overlapping atomic shells that is procured by angular measurements, and the resulting increase in EXAFS sensitivity for the analysis of the in-plane structure of clays.

Fourier-filtered $k^3\chi_{Fe\text{-}Oct1}$ functions in Fig 16a are in phase for $k < 12$ Å^{-1}, but differ by their amplitude. A similar spectral evolution was observed in biotite samples containing variable amounts of Fe and Mg (Manceau et al. 1990). This behavior is typical of a mixing of Fe-Fe and Fe-(Al,Mg) pairs. The wave amplitude is maximum in Garfield, where each Fe atom is surrounded on average by 2.7 Fe + 0.3 (Al,Mg), and decreases when Al,Mg substitutes for Fe as a result of the π phase difference between the waves backscattered by Al,Mg and Fe atoms (Teo 1986). As shown below, this optimum phase contrast associated with the filtering of the Tet1 contribution by angular measurements greatly increases the sensitivity of EXAFS to the determination of the number of nearest octahedral cations. A representative two-shell fit is given in Figure 16b for sample SWa-l, and best-fit values for N_{Fe}, N_{Al}, and interatomic distances

TABLE 7. EXAFS parameters for nearest cation shells

Sample	Fe-Fe			Fe-(Al,Mg)			
	R (≈)	N	σ (≈)	R (≈)	N	σ (≈)	R_p
PV	3.05	2.5	0.06	3.03	0.5	0.06	0.020
SWa-1	3.05	2.0	0.06	3.03	1.0	0.06	0.040

Notes: Fit performed using theoretical amplitude and phase shift functions calculated with FEFF7.02 and calibrated on the Garfield reference. ΔE = –1.5 eV. Fits were performed on spectra recorded at α = 0° after subtraction of the residual Tet1 contribution. *N* are crystallographic values corrected for the angular dependence term.

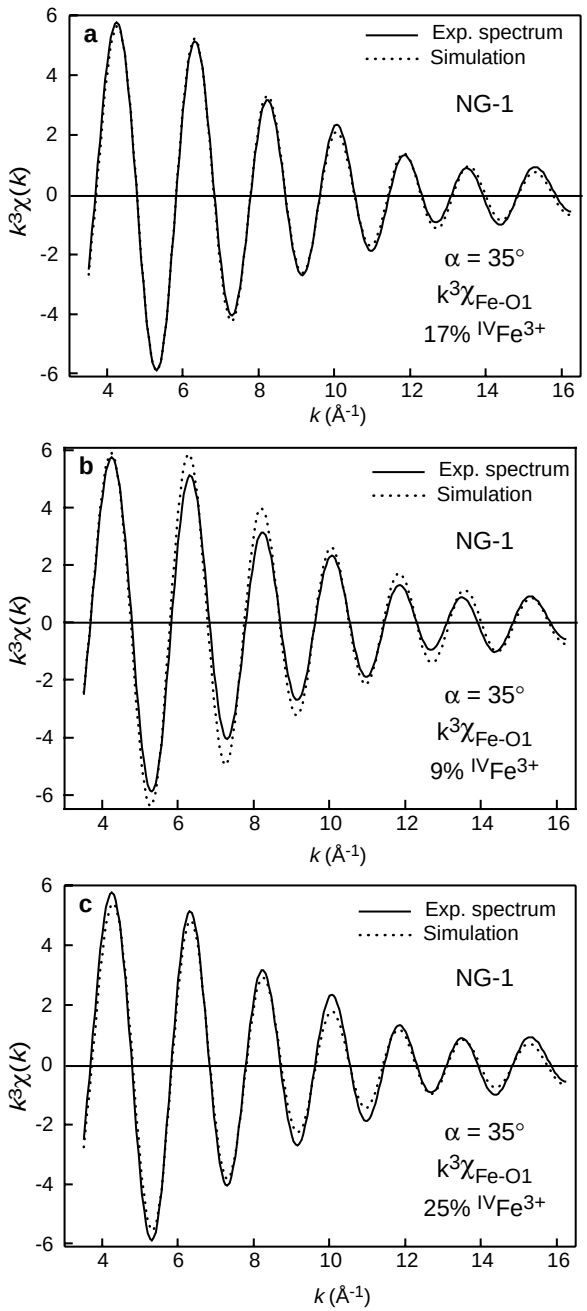

FIGURE 14. (**a**) Best two-shell fit of k^3 $_{Fe\text{-}O1}$ for NG-1 obtained by assuming 17% of $^{IV}Fe^{3+}$. (**b**), (**c**) Spectral simulations assuming 9% and 25% of $^{IV}Fe^{3+}$, respectively.

are given in Table 7. For all samples, the wave envelope was poorly reproduced for k < 5 Å^{-1}, suggesting that the contribution of a third atomic shell has its wave amplitude maximum at low k. This additional contribution is suggestive of the O2 shell, which was incompletely filtered by the FT^{-1} because of the incomplete separation of Oct1 and O2 peaks in the RSFs (Fig. 15b). Two strategies can be adopted for this quantitative analysis. The first consists of performing a Fourier backtransform of the Fe-Oct1 and Fe-O2 contributions (R + ΔR window = 2.2–3.7 Å), followed by a three-shell spectral fit (Fe-Fe1 + Fe-(Al,Mg) 1 + Fe-O2) over the extended wavevector range 3.0 Å^{-1} ≤ k ≤ 14 Å^{-1}. The second strategy is to single out the Oct1 RSF peak (R + ΔR window = 2.2 to 3.0 Å^{-1}), then to perform a two-shell fit [Fe-Fe + Fe-(Al,Mg)] in a reduced k range, typically 4.5 Å^{-1} ≤ k ≤ 14 Å^{-1}. These two procedures were compared and yielded the same structural results. The uncertainty of N_{Fe} and N_{Al} was evaluated for SWa-l by varying their values keeping the N_{Fe}+ N_{Al} sum equals to 3. Figures 16c and 16d show that a 10% variation of N_{Fe} and 20% of N_{Al} results in an approximate fit to the experimental spectrum, with the wave amplitude and envelope being poorly reproduced. The precision on the number of nearest cations is, by all evidence, better than

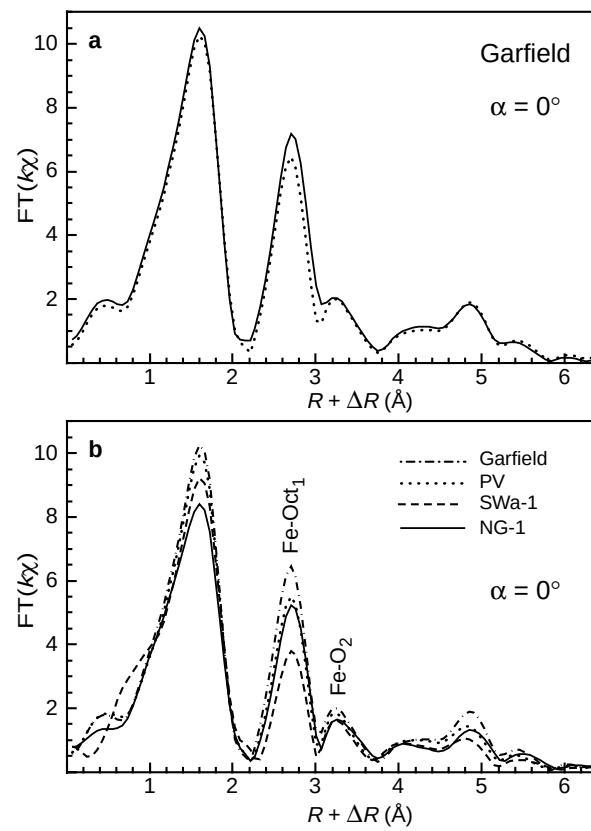

FIGURE 15. (**a**) Comparison of RSF for Garfield nontronite at α = 0° (solid line) to the same RSF obtained after subtraction of the Fe-Tet1 contribution (dotted line). (**b**) Comparison of RSFs for the various nontronite samples at α = 0° after subtraction of the Fe-Tet1 contributions.

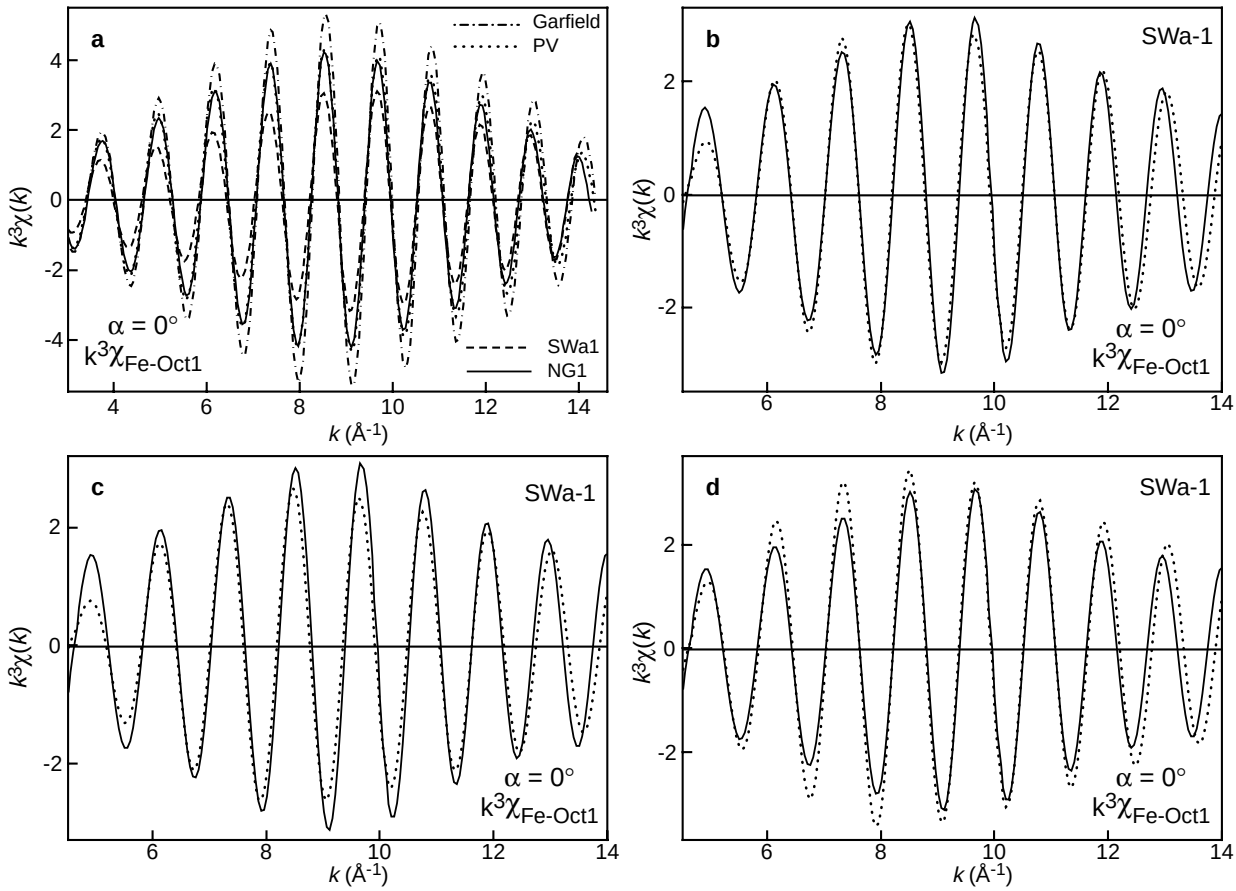

FIGURE 16. (**a**) Fourier filtered Fe-Oct1 contributions to EXAFS for the various nontronite samples. (**b**) Best two-shell fit for SWa-1 assuming N_{Fe} = 2.0 and N_{Al} = 1.0. (**c**) Two-shell fit assuming N_{Fe} = 1.8 and N_{Al} = 1.2. (**d**) Two-shell fit assuming N_{Fe} = 2.2 and N_{Al} = 0.8. For the three spectral simulations, R_{Fe} = 3.05 Å, σ_{Fe} = 0.06 Å, R_{Al} = 3.03 Å, σ_{Al} = 0.06 Å, ΔE = -1.5eV. In **b** to **d** solid lines are experimental spectra and dotted lines are calculated spectra. The R + ΔR window for the inverse Fourier transform in Figure 15b is [2.2–3.0] Å.

20% and possibly slightly better than 10%. In the discussion section this precision will be shown to be sufficient to build a two-dimensional map of the distribution of Fe, Al, and Mg in the octahedral sheet of SWa-l.

DISCUSSION

Structural formulae

Structural formulae calculations show that the layer charge of the four nontronites increases in the order NG-1 < Garfield < SWa-1 < PV, and ranges from 0.69 to 0.91 atoms per unit cell (Table 2). This layer charge is fully balanced by interlayer Na. The distribution and origin of the layer charge between the octahedral and tetrahedral sheets varies significantly from one sample to the next. The source of layer charge is almost uniquely from $^{IV}Al^{3+}$ in Garfield, predominantly from $^{IV}Fe^{3+}$ in NG-1, and from $^{IV}Al^{3+}$ and $^{VI}Mg^{2+}$ in PV and SWa-1. Garfield, SWa-1, and NG-1 are typical nontronites because the source of layer charge is uniquely or predominantly localized in the tetrahedral sheet like in bedeillite. In PV the octahedral charge (0.48) is slightly higher than the tetrahedral charge (0.43).

The customary method of calculating structrual formulae for clay minerals is to first use Al to complete the charge in the tetrahedral sheet, and then to place the balance of the Al in the octahedral sheet. Fe normally is allocated to the tetrahedral sheet only if insufficient Al is present. This approach may not be correct in detail. Chemical analysis of sample NG-1 permits, but does not require, the assignment of Fe^{3+} to the tetrahedral sheet (Table 2). From the above X-ray absorption pre-edge and EXAFS results as much as 14 to 20% of the structural Fe^{3+} fills tetrahedral sites in sample NG-1. This placement can be accommodated in the structural formula calculation by allowing tetrahedral Al to be replaced by Fe^{3+}. The maximum possible substitution of tetrahedral Fe^{3+} for tetrahedral Al in the structural formula of NG-1 coincides with the maximum amount of $^{IV}Fe^{3+}$ allowed by EXAFS (20%). This deviation from the standard convention of assigning the tetrahedral charge primarily to Al^{3+} is not uncommon (Cicel and Komadel 1994), and has been reported in glauconites by IR spectroscopy (Besson and Drits 1997b; Slonimskaya et al. 1986) and smectites by Mossbauer spectroscopy (Cardile 1989).

The formulae reported by Goodman et al. (1976) based on

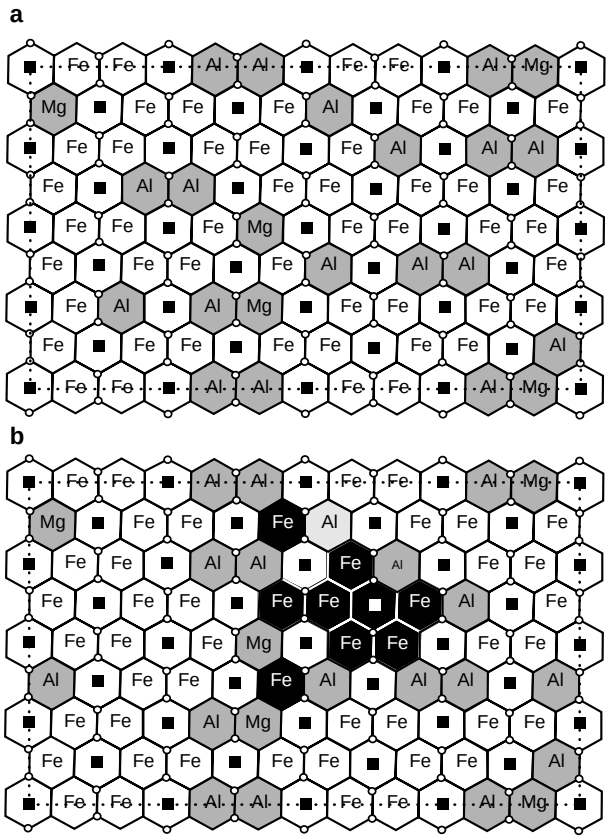

FIGURE 17. Structural model for the two-dimensional distribution of cations in the octahedral sheet of SWa-1. (**a**) (Al,Mg)-(Al,Mg) pairs are dispersed in the Fe^{3+} framework. (**b**) Existence of Fe-rich domains delimited by (Al,Mg)-(Al,Mg) pairs and empty octahedra. In both models, N_{Fe} = 2.05 and $N_{Al,Mg}$ = 0.95.

electron microprobe analysis for Garfield [$(Si_{6.84}Al_{1.05}Fe_{0.11})(Fe^{3+}_{3.96}Mg_{0.04})O_{20}(OH)_4$], SWa-1 [$(Si_{7.30}Al_{0.70})(Fe^{3+}_{2.73}Al_{1.06}Mg_{0.26})O_{20}(OH)_4$], and sample CAL [$(Si_{6.21}Al_{0.14}Fe^{3+}_{1.65})(Fe^{3+}_{4.04})O_{20}(OH)_4$], which is assumed to be similar to PV (both originated in Panamint Valley, California, and were supplied by J.L. Post), deviate from those determined in Table 2. The previous studies reported more total Fe in the clay structure than was found in the current study. This difference is attributed to the presence of Fe oxides (Murad 1987) which can only be removed by careful and repeated washing and fractionation of the sample. Goodman et al. (1976) also attributed more Fe to the tetrahedral sheet in samples Garfield and PV than appears justified in the present study. Bonnin et al. (1985) also reported no tetrahedral Fe in this Garfield sample.

The structural formula of sample NG-1 calculated by Peterson et al. (1987) [$M^{+}_{0.72}(Si_{7.30}Al_{0.48}Fe^{3+}_{0.22})(Fe^{3+}_{3.94}Fe^{2+}_{0.02}Mg_{0.04})O_{20}(OH)_4$] contains 12% more total Fe than in Table 2, which led them to assign some of the Fe to tetrahedral positions. The greater amount of Fe reported by Peterson et al. (1987) is probably due to maghemite remaining after separation (Lear et al. 1988).

Distribution of Fe and (Al,Mg) in the octahedral sheet of SWa-l

The simulation of the XRD powder pattern for SWa-l showed that octahedral cations fill only M2 sites. The actual distribution of (Al,Mg) and Fe in the M2 sites can be modeled by combining results from EXAFS and IR spectroscopy. In self-supporting films, *ab* crystallographic planes of individual platelets are distributed at random in the film plane (Manceau et al. 1998). The EXAFS signal is, therefore, isotropic in the parallel orientation, which means that differentiation of the individual contributions of the three Fe-Oct1 pairs oriented along [010], [$3\bar{1}0$], and [$\bar{3}10$] is impossible (Fig. 1b). Therefore N_{Fe} and $N_{Al,Mg}$ refer to the mean number of nearest Fe and (Al,Mg) cations, averaged over all Fe positions and crystallographic directions. The statistical distribution of Fe and (Al,Mg) may, however, be evaluated comparing N_{Fe} and $N_{Al,Mg}$ EXAFS values to those calculated from the chemical composition assuming a random distribution of cations. This approach has been used previously to study the distribution of Ni in Ni-Mg (Manceau and Calas 1986) and Fe in Fe-Mg (Manceau et al. 1990) phyllosilicates. Al and Mg have a similar backscattering amplitude (F) and phase shift (ϕ), which precludes them from being distinguished at the Fe K-edge. Consequently, the only information recoverable from Fe-EXAFS is the average distribution of Fe relative to light atoms like Al and Mg. The fractions of Fe and $(Al+Mg)_{Oct}$ are 0.67 and 0.33 in SWa-l. Thus, if Fe atoms are randomly distributed, N_{Fe} and $N_{Al,Mg}$ should be equal to 2.0 and 1.0. These values are identical to those derived from the EXAFS analysis (Table 7). In conclusion, based on a precision of 10% for N_{Fe} and 20% for $N_{Al,Mg}$, Fe atoms are statistically distributed in the octahedral sheets of SWa-l.

Occurrence probabilities of cation pairs can also be retrieved by IR through the quantitative analysis of the frequency and intensity of OH stretching modes (Besson et al. 1987; Drits et al. 1997; Slonimskaya et al. 1986). But in contrast to EXAFS, IR is only sensitive to one-dimensional cation distribution in trans-vacant clays. This is apparent in Figure 1b, which shows that cation pairs located in adjacent octahedra in the proximity of OH groups are oriented along *b*. Another important difference from EXAFS is that IR has no atomic selectivity and, therefore, detects all existing pairs, whereas Fe-EXAFS is only sensitive to Fe-Fe and Fe(Al,Mg) pairs, without distinction between Fe-Al and Fe-Mg, and is blind to Al-Mg pairs. Thus, IR and P-EXAFS are clearly two complementary and extremely useful techniques for the investigation of the actual distribution of cations in the octahedral sheets of clays, as recently illustrated by Muller et al. (1997) on montmorillonite and Drits et al. (1997) on celadonites, glauconites, and Fe-illites. This dual approach can be applied to SWa-l by using the IR data published by Madejova et al. (1994), in spite of the fact that the SWa-1 samples studied by IR and EXAFS were prepared with different degrees of purification. The sample used by Madejova et al. (1994) had a slight amount of Fe oxide impurity, which would translate into a Fe fraction of 0.706 compared to 0.67 in the present sample, corresponding respectively to N_{Fe} values of 2.1 and 2.0 for a statistical distribution. We have no reason to suspect that Fe would be distributed differently in the phyllosilicate layers of these two samples and, con-

sequently, the following logically assumes that N_{Fe} = 2.1 and $N_{Al,Mg}$ = 0.9 in the sample of Madejova et al. (1994). Note also that the difference between N_{Fe} = 2.1 and 2.0 is typically within the uncertainty on N which means that EXAFS is insensitive to this slight difference in chemical composition.

Madejova et al. (1994) showed that the distribution of cations along *b* is not random, Fe-Fe, Al-Al, and Al-Mg pairs having a greater, and Fe-(Al,Mg) a lesser, probability than predicted from statistics. In contrast, EXAFS data indicate that, when averaged along the three layer directions, the number of Fe-Fe and Fe-(Al,Mg) pairs follows statistics. These two contrasting results simply indicate that Fe-Fe and (Al,Mg)-(Al,Mg) pairs are preferentially aligned along *b* and Fe-(Al,Mg) along [$\bar{3}10$] and [$3\bar{1}0$]. A two-dimensional model for the distribution of cations in the octahedral sheet of SWa-l is illustrated in Figure 17a. The rectangle is comprised of 16 unit cells and contains 45 Fe, 15 Al, and 4 Mg, in agreement with the structural formula of Madejova et al. (1994), and 19 Fe-Fe, 5 Fe-Al, 4 Al-Al, 2 Fe-Mg, and 2 Al-Mg pairs in accordance with IR. To satisfy both the IR and EXAFS data, one is forced to place all (Al,Mg)-(Al,Mg) pairs in the [010] direction and to surround them with Fe atoms, thereby creating Fe-(Al,Mg) pairs in the other two directions. For the model represented in Figure 17a, N_{Fe} and $N_{Al,Mg}$ are equal to 2.05 and 0.95, and are thus almost identical to the theoretical values, 2.1 and 0.9.

One may notice that this pattern contains (Al,Mg) pairs and one (Al,Mg) triplet, but is devoid of larger clusters of light atoms. Values for N_{Fe} and $N_{Al,Mg}$ are particularly sensitive to the distribution of (Al,Mg) atoms in the layer. Two limiting cases can be envisaged: a complete dilution of (Al,Mg) atoms within a Fe^{3+} network with no (Al,Mg)-(Al,Mg) pairs; or a complete segregation of (Al,Mg) atoms. The former situation corresponds to the minimum value of N_{Fe} and to the maximum of $N_{Al,Mg}$, and the reverse is true for the latter situation. Calculations for the first case reveal that N_{Fe}(min) = 1.8 and $N_{Al,Mg}$(max) = 1.2, and for the second, N_{Fe}(max) = 2.7 and $N_{Al,Mg}$(min) = 0.3. The presumed N values (N_{Fe} = 2.1 and $N_{Al,Mg}$ = 0.9) are closer to the first situation, which indicates that (Al,Mg)-(Al,Mg) pairs are merely isolated, and if (Al,Mg) clusters exist they are few. Thus, the combination of IR and EXAFS results leads to the conclusion that, in SWa-l, (Al,Mg) pairs are predominantly, if not uniquely, oriented along *b* and that these pairs are surrounded by Fe atoms in the [$\bar{3}10$] and [$3\bar{1}0$] directions. This two-dimensional pattern accounts for the departure from the one-dimensional random distribution along the *b* axis observed by IR, and specifically for the lower probability of Fe-Al pairs in this crystallographic direction.

The pattern of Figure 17a was established by distributing the (Al,Mg)-(Al,Mg) pairs at random within the Fe^{3+} framework. Figure 17b shows that placement of pairs of light atoms delimiting small ferruginous domains is also possible (N_{Fe} = 2.05 and $N_{Al,Mg}$ = 0.95 as in the previous model). This alternative model would provide an explanation for the lack of long range magnetic ordering in SWa-1 at 1.3 K (Lear and Stucki 1990), as magnetic Fe^{3+} domains are separated from each other by diamagnetic cations and vacant M1 sites. Using the predictions of percolation theory (Stauffer 1979), Lear and Stucki (1990) contemplated this structural interpretation for explaining the non-ideal antiferromagnetic behavior of SWa-l at low temperature, but in the absence of experimental data concerning the distribution of octahedral cations in this mineral, a model with a partial occupation of trans sites, in which anti-ferromagnetic frustration occurred, was their preferred explanation. Based on XRD results presented here, however, which showed that SWa-l nontronite consists of tv 2:1 layers, the existence of small magnetic domains separated by diamagnetic cations is the more probable reason for the observed magnetic properties of SWa-l nontronite.

ACKNOWLEDGMENTS

E. Curti, A. Scheidegger, and S. Traina are acknowledged for their reviews, and R.A. Eggleton is thanked for his editorial handling. The authors thank the staff at LURE for operating the synchrotron facility, and specifically Agnès Traverse for running the D42 spectrometer. A.M. acknowledges the University of Illinois at Urbana-Champaign for a George A. Miller Endowment fellowship. D.C. acknowledges H.R. Wenk and M. Pernet for access to the texture experiments at the Department of Geology and Geophysics, University of California-Berkeley, and Laboratoire de Cristallographie, Grenoble, France, respectively. W.G. acknowledges the French Consulate for a bourse Chateaubriand. J.W.S. acknowledges the Illinois Council for Food and Agricultural Research for partial funding of this study and J.L. Post, University of California, Sacramento, for supplying the unpurified Panamint Valley sample. V.A.D. acknowledges the Russian Science Fundation for partial funding of this study.

REFERENCES CITED

Arnod, H. (1986) Crystal structure of $FePO_4$ at 294 and 20K. Zeitschrift für Kristallographie, 177, 139–142.

Barnhisel, R. and Bertsch, P.M. (1982) Aluminum. In A.L. Page, Ed., Methods of Soil Analysis, Part 2, Chemical and Microbiological Properties, p. 288–290. Soil Science Society of America, Madison.

Besson, G. and Drits, V.A. (1997a) Refined relationships between chemical composition of dioctahedral fine-grained mica minerals and their infrared spectra within the OH stretching region. Part I: Identification of the OH stretching bands. Clays and Clay Minerals, 45, 158–169.

———(1997b) Refined relationships between chemical composition of dioctahedral fine-grained mica minerals and their infrared spectra within the OH stretching region. Part II: The main factors affecting OH vibrations and quantitative analysis. Clays and Clay Minerals, 45, 170–183.

Besson, G., Bookin, A.S., Dainak, L.G., Rautureau, M., Tsipursky, S.I., Tchoubar, C., and Drits, V.A. (1983) Use of diffraction and Mössbauer methods for the structural and crystallochemical characterization of nontronites. Journal of Applied Crystallography, 16, 374–183.

Besson, G., Drits, V.A., Daynyak, L.G., and Smoliar, B.B. (1987) Analysis of cation distribution in dioctahedral micaceous minerals on the basis of IR spectroscopy data. Clay Minerals, 22, 465–478.

Bonnin, D., Calas, G., Suquet, H., and Pezerat, H. (1985) Sites occupancy of Fe^{3+} in Garfield nontronite: A spectroscopic study. Physics and Chemistry of Minerals, 12, 55–64.

Brindley, G.W. and Brown, G. (1980) Crystal structures of clay minerals and their X-ray identification, 495 p. Mineralogical Society, London.

Bunge, H.J. (1981) Textures in Materials Science, 551 p. Butterworths, London.

Cardile, C.M. (1989) Tetrahedral iron in smectite: a critical comment. Clays and Clay Minerals, 37, 185-188.

Cicel, B. and Komadel, P. (1994) Structural formulae of layer silicates. In J.E. Amonette and L.W. Zelazny, Eds., Quantitative Methods in Soil Mineralogy, p. 114–136. Soil Science Society of America, Madison.

Douglas, B., McDaniel, D., and Alexander, J. (1994) Concepts and models of inorganic chemistry, 928 p. Wiley, New York.

Drits, V.A. and McCarty, D.K. (1996) The nature of diffraction effects from illite and illite-smectite consisting of interstratified trans-vacant and cis-vacant 2:1 layers: A semiquantitative technique for determination of layer-type content. American Mineralogist, 81, 852–863.

Drits, V.A. and Tchoubar, C. (1990) X-ray diffraction by disordered lamellar structures: Theory and applications to microdivided silicates and carbons, 371 p. Springer Verlag, Berlin.

Drits, V.A., Plançon, A., Sakharov, B.A., Besson, G., Tsipursky, S.I., and Tchoubar, C. (1984) Diffraction effects calculated for structural models of K-saturated montmorillonite containing different types of defects. Clay Minerals, 19, 541–561.

Drits, V.A., Salyn, A.L., and Sucha, V. (1996) Structural transformations of interstratified illite-smectites from Dolna Ves hydrothermal deposits: Dynamics and mechanisms. Clays and Clay Minerals, 44, 181–190.

Drits, V.A., Dainyak, L.G., Muller, F., Besson, G., and Manceau, A. (1997) Isomor-

phous cation distribution in celadonites, glauconites and Fe-illites determined by infrared, Mossbauer and EXAFS spectroscopies. Clay Minerals, 32, 153–179.
Farges, F., Brown, G.E., and Rehr, J.J. (1997) Ti K-edge XANES studies of Ti coordination and disorder in oxide compounds: Comparison between theory and experiment. Physical Review, 56, 1809–1819.
Goodman, B.A., Russell, J.D., Fraser, A.R., and Woodhams, F.W.D. (1976) A Mössbauer and IR spectroscopic study of the structure of nontronite. Clays and Clay Minerals, 24, 53–59.
Güven, N. (1991) Smectites. In Mineralogical Society of America Reviews in Mineralogy, 19, 497–560.
Hallmark, C.T., Wilding, L.P., and Smeck, N.E. (1982) Silicon. In A.L. Page, Ed., Methods of Soil Analysis, Part 2, Chemical and Microbiological Properties, p. 263–274. Soil Science Society of America, Madison.
Hazemann, J.L., Manceau, A., Sainctavit, P., and Malgrange, C. (1992) Structure of the $\alpha Fe_xAl_{1-x}OOH$ solid solution. I. Evidence by polarized EXAFS for an epitaxial growth of hematite-like clusters in diaspore. Physics and Chemistry of Minerals, 19, 25–38.
Komadel, P. and Stucki, J.W. (1988) The quantitative assay of minerals for Fe^{2+} and Fe^{3+} using 1,10-phenanthroline. III. A rapid photochemical method. Clays and Clay Minerals, 36, 379–381.
Lear, P.R. and Stucki, J.W. (1990) Magnetic properties and site occupancy of iron in nontronite. Clay Minerals, 25, 3–14.
Lear, P.R., Komadel, P., and Stucki, J.W. (1988) Mossbauer spectrosocopic identification of iron oxides in nontronite form Hohen Hagen, Federal Republic of Germany. Clays and Clay Minerals, 376–378.
Lengeler, B. and Eisenberger, P. (1980) Extended x-ray absorption fine structure analysis of interatomic distances, coordination numbers, and mean relative displacements in disordered alloys. Physical Review, B21, 4507–4528.
Lu, K. and Stern, E.A. (1983) Size effect of powdered sample on EXAFS amplitude. Nuclear Instruments and Methods, 212, 475–478.
Madejova, J., Komadel, P., and Cicel, B. (1994) Infrared study of octahedral site populations in smectites. Clay Minerals, 29, 319–326.
Manceau, A. (1990) Distribution of cations among the octahedra of phyllosilicates: insight from EXAFS. Canadian Mineralogist, 28, 321–328.
——(1995) The mechanism of anion adsorption on Fe oxides: Evidence for the bonding of arsenate tetrahedra on free $Fe(O,OH)_6$ edges. Geochimica et Cosmochimica Acta, 59, 3647–3653.
Manceau, A. and Calas, G. (1986) Ni-bearing clay minerals. 2. X-ray absorption study of Ni-Mg distribution. Clay Minerals, 21, 341–360.
Manceau, A. and Combes, J.M. (1988) Structure of Mn and Fe oxides and oxyhydroxides: a topological approach by EXAFS. Physics and Chemistry of Minerals, 15, 283–295.
Manceau, A. and Gates, W. (1997) Surface structural model for ferrihydrite. Clays and Clay Minerals, 448–460.
Manceau, A., Bonnin, D., Kaiser, P., and Frétigny, C. (1988) Polarized EXAFS of biotite and chlorite. Physics and Chemistry of Minerals, 16, 180–185.
Manceau, A., Bonnin, D., Stone, W.E.E., and Sanz, J. (1990) Distribution of Fe in the octahedral sheet of trioctahedral micas by polarized EXAFS. Comparison with NMR results. Physics and Chemistry of Minerals, 17, 363–370.
Manceau, A., Combes, J.M., and Calas, G. (1990b) New data and a revised model for ferrihydrite:A comment on a paper by R. A. Eggleton and R. W. Fitzpatrick. Clays and Clay Minerals, 38, 331–334.
Manceau, A., Chateigner, D., and Gates, W.P. (1998) Polarized EXAFS, distance-valence least-squares modeling (DVLS) and quantitative texture analysis approaches to the structural refinement of Garfield nontronite. Physics and Chemistry of Minerals, 25, 347–365.
Manceau, A., Schlegel, M., Chateigner, D., Lanson, B., Bartoli, C., and Gates, W.P. (1999) Application of Polarized EXAFS to Fine-Grained Layered Minerals. In D. Schulze, P. Bertsch and J. Stucki, Eds., Synchrotron X-ray Methods in Clay Science, Clay Mineral Society of America, 9, 69–114.
Manceau, A., Drits, V.A., Lanson, B., Chateigner, D., Wu, J., Huo, D., Gates, W.P., and Stucki, J.W. (2000) Oxidation-reduction mechanism of iron in dioctahedral smectites. 2. Structural chemistry of reduced Garfield nontronite. American Mineralogist, **{rachel to fill in on pages; Auth: add citation in text!}**
Matthies, S.M., Vinel, G.W., and Helming, K. (1987) In S.M. Matthies, Eds., Standard Distributions in Texture Analysis, p. 78–87. Akademie Verlag, Berlin.
McCarty, D.K. and Reynolds, R.C. (1995) Rotationally disordered illite-smectite in Paleozoic K-bentonites. Clays and Clay Minerals, 43, 271–284.
Muller, F., Besson, G., Manceau, A., and Drits, V.A. (1997) Distribution of isomorphous cations within octahedral sheets in montmorillonite from Camp-Bertaux. Physics and Chemistry of Minerals, 24, 159–166.
Muller, J.E., Jepson, O., and Wilkins, J.W. (1982) X-ray absorption spectra: K-edges of 3d transitions metals L-edges of 3d and 4d metals, and M-edges of palladium. Solid State Communication, 42, 365–368.
Murad, E. (1987) Mössbauer spectra of nontronites: structural implications and characterization of associated iron oxides. Zeitschrift für Pflanzenernaehrung und Bodenkunde, 279–285.
Murad, E., Cashion, J.D., and Brown, L.J. (1990) Magnetic ordering in Garfield nontronite under applied magnetic fields. Clay Minerals, 25, 261–270.
Plançon, A. (1981) Diffraction by layer structure containing different kinds of layers and stacking faults. Journal of Applied Crystallography, 14, 300–304.
Radoslovich, E.W. (1962) The cell dimensions and symmetry of layer-lattice silicates. II. Regression relations. American Mineralogist, 47, 617–636.
Rehr, J.J., Mustre de Leon, J., Zabinsky, S.I., and Albers, R.C. (1991) Theoretical x-ray absorption fine structure standards. Journal of the American Chemical Society, 113, 5135–5145.
Sakharov, B.A., Besson, G., Drits, V.A., Kameneva, M.Y., Salyn, A.L., and Smoliar, B.B. (1990) X-ray study of the nature of stacking faults in the structure of glauconites. Clay Minerals, 25, 419–436.
Sakharov, B.A., Naumov, A.S., and Drits, V.A. (1982a) X-ray diffraction by mixed-layer structures with random distribution of stacking faults. Dokladi Akademie Naukia SSSR, 265, 339–343.
Sakharov, B.A., Naumov, A.S., and Drits, V.A. (1982b) X-ray intensities scattered by layer structure with short range ordering parameters S≥1 and G≥1. Dokladi Akademie Naukia SSSR, 265, 871–874.
Slonimskaya, M., Besson, G., Dainyak, L.G., Tchoubar, C., and Drits, V.A. (1986) Interpretation of the IR spectra of celadonites and glauconites in the region of OH-stretching frequencies. Clay Minerals, 21, 377–388.
Smoliar-Zviagina, B.B. (1993) Relationships between structural parameters and chemical composition of micas. Clay Minerals, 28, 603–624.
Stauffer, J. (1979) Scaling theory of percolation clusters. Physical Review, 54, 1–74.
Stern, E.A., and Kim, K. (1981) Thickness effect on the extended x-ray absorption fine structure amplitude. Physical Review, B23, 3781–3787.
Stucki, J.W. (1988) Structural iron in smectites. In J.W. Stucki, B.A. Goodman and U. Schwertmann, Eds., Iron in Soils and Clay Minerals, p. 625–676. Riedel Publishing Company, 217.
Teo, B.K. (1986) EXAFS: Basic Principles and Data Analysis, 349 p. Springer-Verlag, Berlin.
Tsipursky, S.I. and Drits, V.A. (1984) The distribution of cations in the 2:1 layers of dioctahedral smectites studied by oblique-texture electron diffraction. Clay Minerals, 19, 177–193.
Tsipursky, S.I., Drits, V.A., and Checkin, S.S. (1978) Study of structural ordering of nontronite by oblique texture electron diffraction. Investiya Akademie Nauk, SSSR, Seriya Geologicheskaya, 10, 105–113.
Tsipursky, S.I., Drits, V.A., and Plançon, A. (1985) Calculation of the intensities distribution in oblique texture electron diffraction patterns. Kristallografiya, 30, 38–44.

MANUSCRIPT RECEIVED AUGUST 3, 1998
MANUSCRIPT ACCEPTED AUGUST 15, 1999
PAPER HANDLED BY R.A. EGGLETON